were found to be up to 30 times greater than from non-parasitized red blood cells. Complete inhibition of GloI for 24 h was previously estimated to translate into a methylglyoxal concentration of 0.3 M in the infected erythrocyte (Vander Jagt *et al.*, 1990). Various glutathione-derived glyoxalase-substrate analogues inhibited recombinant glyoxalases, and the growth of *P. falciparum* blood stages (Thornalley *et al.*, 1994; Akoachere *et al.*, 2005).

The compounds methyl-gerfelin (MGFN) and curcumin were recently shown to be non-glutathione inhibitors of small homodimeric mammalian GloI: MGFN and the natural compound gerfelin (GFN) from the fungus *Beauveria felina* inhibited mouse GloI in a competitive manner with a K_i^{app} of ~0.2 μM (Kawatani *et al.*, 2008). Curcumin from the plant *Curcuma longa* is discussed to interact with more than 30 proteins resulting in antioxidant, antimicrobial, anti-inflammatory, anti-proliferative and pro-apoptotic effects (Aggarwal and Sung, 2009). Curcumin also inhibited human GloI with a K_i^{app} of ~5 μM (Santel *et al.*, 2008). An anti-malarial activity of curcumin was previously shown for *P. falciparum* cell cultures and for the rodent parasite *Plasmodium berghei* in vivo (Reddy *et al.*, 2005; Nandakumar *et al.*, 2006; Cui *et al.*, 2007), although these effects were not assigned to the glyoxalase system.

Here we studied the glyoxalases from *P. falciparum* in cell culture and in recombinant form. We determined the cellular localization of GloI, cGloII and tGloII and analysed the formation of homo- and hetero-oligomers for GloI and cGloII. In addition, we asked if, and to what extend, MGFN inhibits GloI and the blood stages of *P. falciparum* and compared the effects with curcumin. We revealed an apicoplast localization for tGloII whereas GloI and cGloII were found to form a cytosolic glyoxalase system. The cytosolic enzyme couple did not seem to interact but cGloII occurred in an unexpected monomer–dimer equilibrium. Furthermore, growth of *P. falciparum* blood stages was inhibited by MGFN, and curcumin and MGFN were both competitive inhibitors of GloI but interacted in a different manner with the two active sites of the monomeric enzyme.

Results

Subcellular localization of the three glyoxalases

GloI and cGloII both lack any obvious protein targeting signals and are thought to be cytosolic proteins. tGloII was previously suggested to contain a targeting signal based on *in silico* analyses (Akoachere *et al.*, 2005). Using different programmes we got rather low probability scores for predicted targeting sequences of tGloII. For example, a value of only 0.26 (out of 1.0) was obtained with PATS 1.2.1 (Zuegge *et al.*, 2001) for the prediction of a so-called bipartite topogenic signal required for apicoplast import. To investigate the true localization of the glyoxalases we expressed GloI, cGloII and tGloII as green fluorescent protein (GFP) fusion proteins in blood stage parasites. Following transfection and selection with 2.5 nM WR99210, a drug-resistant parasite population was obtained after 19–25 days (hereafter referred to as $3D7^{GloIG}$, $3D7^{cGloIIG}$ and $3D7^{tGloIIG}$). Epifluorescence microscopy of erythrocytes infected with $3D7^{GloIG}$ or $3D7^{cGloIIG}$ revealed GFP fluorescence only within the body of the parasite (Fig. 1A). In contrast, red blood cells infected with $3D7^{tGloIIG}$ showed GFP fluorescence in a pattern reminiscent of an apicoplast localization (Fig. 1B). This was especially clear in merozoite stage parasites, where each individual merozoite contains one fluorescent 'dot' (Fig. 1B, lower panels). To verify this, we carried out immunolocalization studies with antibodies raised against the acyl carrier protein (ACP), an apicoplast marker (Tonkin *et al.*, 2004). Indeed, we observed a high degree of colocalization between the GFP and ACP signal in both trophozoite (Fig. 1C, upper panels) and schizont stage parasites (Fig. 1C, lower panels), confirming that tGloII-GFP is transported to the apicoplast. In some erythrocytes infected with $3D7^{tGloIIG}$ we also observed a weaker fluorescent signal surrounding the body of the parasite (white arrow in Fig. 1B), probably representing the parasitophorous vacuole. This may be the result of overexpression of the GFP fusion protein, causing overloading of the apicoplast import pathway and thus allowing a portion of our chimeric protein to follow the default secretory pathway to the lumen of the parasitophorous vacuole. Western blot analysis of protein fractions derived from $3D7^{GloIG}$, $3D7^{cGloIIG}$ and $3D7^{tGloIIG}$ infected erythrocytes showed that all these transgenic parasites expressed GFP-chimera proteins of the predicted molecular mass (Fig. 1D). For tGloII-GFP an additional lower band was observed that probably reflects the imported mature protein following cleavage of both signal and apicoplast transit peptide. Additionally a ~26 kDa band could be visualized, probably representing a commonly observed degradation of GFP fusion proteins (Waller *et al.*, 2000).

cGloII forms transient homodimers in solution

When we analysed the apparent molecular mass of previously described cGloII glutathione-binding site mutants (Urscher and Deponte, 2009) by gel filtration chromatography, we were surprised to find lower values for all mutant enzymes than for the wild-type enzyme (Table 1; Fig. 2A). Misfolding of the proteins would have resulted in a higher apparent molecular mass and was previously excluded by CD spectroscopy (Urscher and Deponte, 2009). Plausible causes for the different apparent molecular masses were therefore: (i) altered structural flexibilities and/or (ii) altered monomer–dimer equilibria. Depending

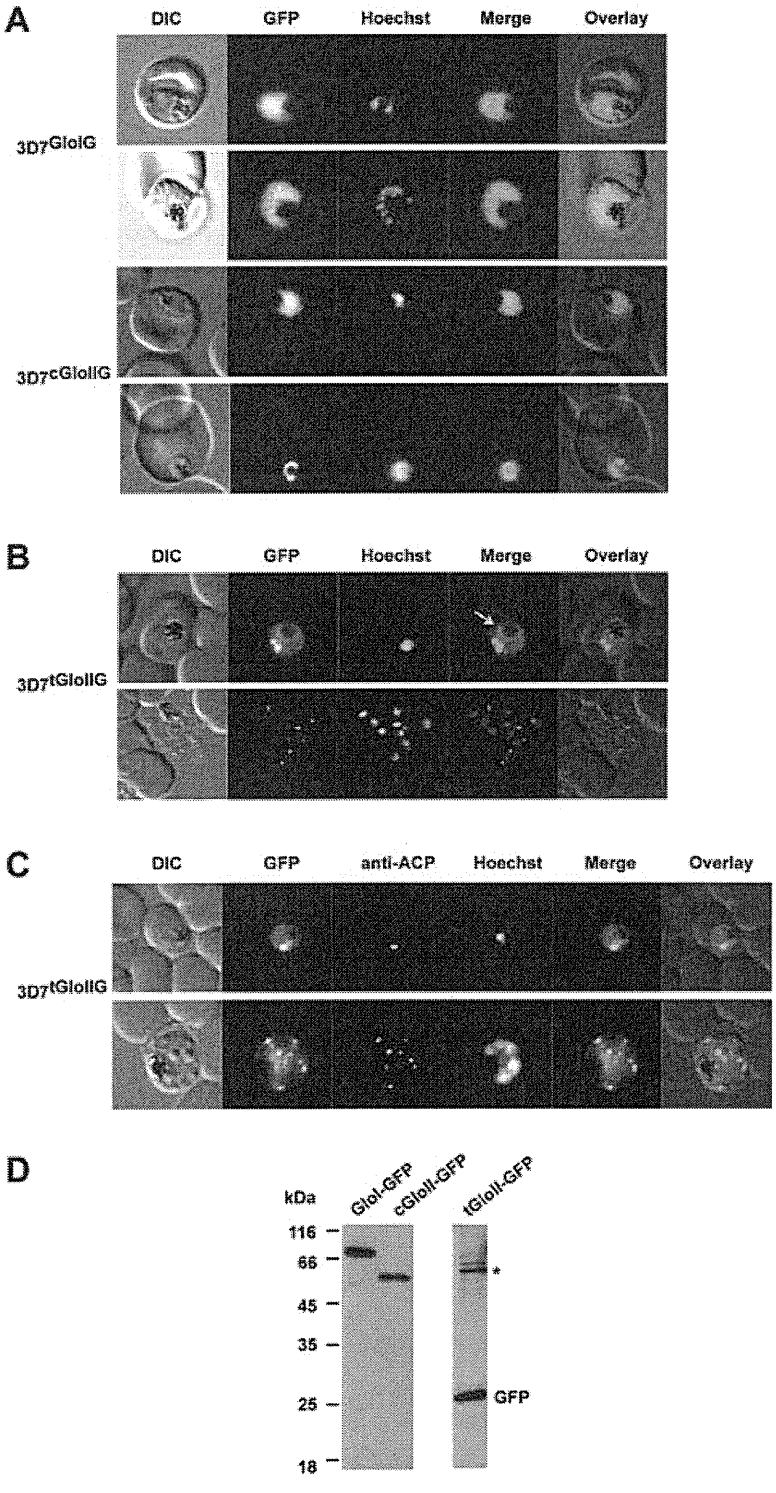

Fig. 1. Localization of GloI, cGloII and tGloII GFP fusion constructs in infected erythrocytes.
A. Live cell imaging of erythrocytes infected with transgenic parasite lines 3D7^{GloIG} (upper panels) and 3D7^{cGloIIG} (lower panels). GFP fluorescence was evident only within the body of the parasite (excluding the food vacuole).
B. Live cell imaging of erythrocytes infected with 3D7^{tGloIIG}. A distinct fluorescent 'dot' was seen in both trophozoite (upper panels) and merozoite (lower panels) stage parasites, indicative of an apicoplast localization. The white arrow shows additional low levels in the parasitophorous vacuole.
C. Colocalization of tGloII-GFP and the apicoplast marker ACP in fixed, immunodecorated cells. Note the high degree of overlap between tGloII-GFP and ACP.
D. Detection of fusion constructs in transgenic parasites by Western blot analysis against the GFP moiety. The calculated molecular masses for GloI-GFP, cGloII-GFP and tGloII-GFP (of 69.6, 57.7 and 65.6 kDa, respectively) were in perfect agreement with the obtained signals. Additional bands at approximately 60 and 26 kDa were observed for tGloII-GFP. The star and the GFP label probably reflect successfully imported and degraded protein subpopulations respectively.

on the association and dissociation rates, different oligomerization states are sometimes not resolved by gel filtration chromatography (e.g. Deponte and Becker, 2005; Nickel *et al.*, 2006). In order to test this hypothesis for cGloII, we performed cross-linking experiments with glutaraldehyde and disuccinimidyl suberate (DSS) (Fig. 2B). The formation of cross-linked homodimers was observed for wild-type cGloII and the mutant cGloII^{R154K}. Longer incubation periods with glutaraldehyde also led to the formation of tetramers. No trimers were detected suggesting that α_2 but not α_3 units were formed. Comparative cross-linking kinetics of cGloII^{R154K} and wild-type enzyme

Table 1. Gel filtration chromatography of wild-type cGloII and mutant enzymes.

Enzyme	M_{app} (kDa)[a]	M_{app}/31.8 kDa
cGloII WT	45.3 ± 2.0	1.43 ± 0.06
cGloII^{R154K}	23.2 ± 1.6	0.73 ± 0.05
cGloII^{R154M}	26.9 ± 8.1	0.85 ± 0.26
cGloII^{R257Q}	39.0 ± 0.2	1.23 ± 0.01
cGloII^{R257D}	26.1 ± 2.1	0.82 ± 0.07
cGloII^{K260Q}	32.0 ± 0.2	1.01 ± 0.01
cGloII^{K260D}	37.5 ± 2.1	1.18 ± 0.07

a. The apparent molecular mass (M_{app}) was averaged from two to four independent gel filtration experiments (e.g. Fig. 2A). The theoretical molecular mass of recombinant MRGS(H)$_6$GS-tagged wild-type enzyme and glutathione-binding site mutants (Urscher and Deponte, 2009) is 31.8 kDa.

revealed a slower appearance of cross-linked cGloII^{R154K} dimers (Fig. 2B, right panel). Interpreting the slower appearance as a decreased subunit interaction, the result is in accordance with the lower apparent molecular mass of the mutant enzyme as determined by gel filtration chromatography (Table 1; Fig. 2A). Dimer formation was also confirmed by analytical ultracentrifugation (data not shown) and pull-down assays (Fig. 2C): protein A-tagged cGloII co-eluted with His-tagged cGloII from a Ni-NTA column and His-tagged cGloII co-eluted with protein A-tagged cGloII from an IgG-sepharose column. In the absence of the binding partner, no significant unspecific binding was observed for the negative controls. In order to quantify the cGloII subunit interaction, we performed DSS cross-linking experiments with different protein concentrations at 37°C yielding an estimation of the apparent dissociation constant (K_d^{app}) of ~5 μM (Fig. 2D). In summary, cGloII is able to form dimers in solution and exists in a rapid monomer–dimer equilibrium that cannot be resolved by gel filtration chromatography.

We also analysed the potential formation of GloI-cGloII hetero-oligomers. Although both proteins co-eluted on the gel filtration column, no interaction was observed in analytical ultracentrifugation studies as well as pull-down assays using His-tagged GloI and protein A-tagged cGloII and *vice versa* (data not shown). Thus, direct complex formation or even substrate channelling seem to be unlikely for the cytosolic enzyme couple.

Methyl-gerfelin and curcumin as P. falciparum *GloI inhibitors*

The potential inhibitors curcumin and MGFN were tested with recombinant GloI. Both compounds could mimic the enediolate reaction intermediate of the hemithioacetal between methylglyoxal and GSH (Fig. 3A). We therefore analysed the steady-state kinetics of GloI at different concentrations of substrate and inhibitors. Inhibition patterns with curcumin were found to be quite complex: Lineweaver-Burk plots pointed to a competitive inhibition with a rather constant maximum reaction velocity (Fig. 3B). Indeed, curcumin inhibition became insignificant at a substrate concentration ≥ 0.25 mM (Fig. 3C). Based on the slopes of the Lineweaver-Burk plots we generated a secondary plot to determine the K_i value (Segel, 1993). In contrast to a simple competitive inhibition, the secondary plot revealed no straight line. We therefore estimated two apparent K_i values (K_i^{app}) of ~25 μM and > 0.2 mM for low and high curcumin concentrations respectively (Fig. 3D). Similar values were estimated from the non-linear Dixon plots (Fig. 3E). The inhibition patterns might have been caused by different inhibitors such as curcumin and a curcumin–glutathione conjugate (Awasthi *et al.*, 2000). We therefore compared the activity in assays where the inhibitor was either pre-incubated for 1 or 5 min or was added just after the enzyme. Reaction rates of the controls were identical (Fig. S1) indicating that the formation of a curcumin–glutathione conjugate is irrelevant under the chosen assay conditions. More likely, the inhibition patterns are due to the two different active sites of the monomeric enzyme (Deponte *et al.*, 2007). Accordingly, the two K_i^{app} values could reflect inhibitor binding to the high- and the low-affinity binding site. The observation that the enzymatic activity was ~50% even at low substrate and high inhibitor concentrations (Fig. 3C) can then be interpreted as preferential, almost complete inhibition of one of the active sites whereas the other reaction centre remained functional. Indeed, analysing the initial reaction velocity of the mutant enzyme GloI^{E345Q} with 20 μM substrate in the presence of 0–100 μM curcumin did not reveal an immediate inhibition (Fig. S2). Under the same conditions the wild-type enzyme was significantly affected (Figs 3C and S2). GloI^{E345Q} has a functional low-affinity binding site and an inactive reaction centre at the high-affinity binding site (Deponte *et al.*, 2007). The lack of an immediate inhibition of GloI^{E345Q} suggests that curcumin preferentially binds to the high-affinity site, which was already inactivated in the mutant but not in the wild-type enzyme (Fig. S2).

Lineweaver-Burk plots with MGFN also suggested a competitive inhibition (Fig. 3F). The inhibitor was far more efficient than curcumin, as similar residual activities were obtained with less than a tenth of inhibitor. Moreover, a substrate concentration of 0.25 mM was insufficient to regain the maximum reaction velocity (Fig. 3G). The two K_i^{app} values of ~2 and 6 μM for low and high MGFN concentrations were quite similar (Fig. 3H) suggesting that both active sites were inhibited by MGFN. The Dixon plots for MGFN were again non-linear (Fig. 3I) supporting the theory that interactions between the inhibitor and the different active sites and/or conformations of the monomeric enzyme are distinguishable. In summary, MGFN is a more

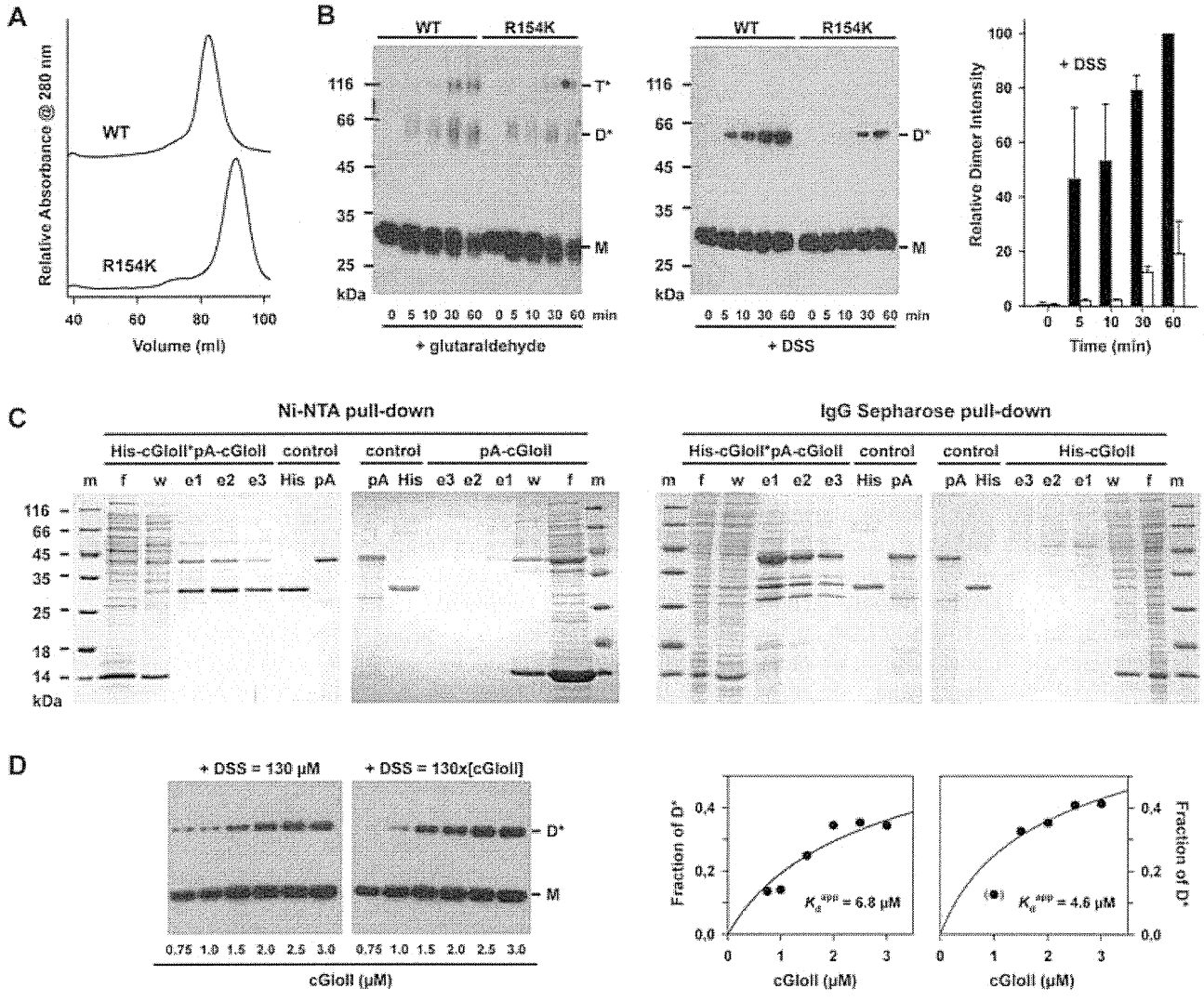

Fig. 2. Gel filtration chromatography, cross-linking and pull-down experiments with cGloII.

A. The apparent molecular mass of purified His-tagged wild-type (WT) enzyme and glutathione-binding site mutants (Urscher and Deponte, 2009) was compared by gel filtration chromatography. All glutathione-binding site mutants eluted at a lower apparent molecular mass than wild-type enzyme (Table 1). Representative gel filtration chromatograms of wild-type cGloII and cGloII^{R154K} are shown for comparison.

B. Cross-linking kinetics with glutaraldehyde and DSS were determined with wild-type enzyme and cGloII^{R154K}. Samples were analysed by reducing SDS-PAGE (12%) and Western blotting against the N-terminal His-tag (left panels). M, monomer; D*, dimer; T*, tetramer. Using different exposure times, signals from the Western blots were quantified and relative intensities of the dimer bands of wild-type enzyme (black bars) and cGloII^{R154K} (white bars) were plotted versus time (right panel).

C. Pull-down experiments with N-terminally His-tagged (His-) and protein A-tagged (pA-) cGloII. The protein A-tagged protein was co-purified by Ni-NTA affinity chromatography (left panel) and the His-tagged protein was co-purified by IgG-sepharose affinity chromatography (right panel). Samples were analysed by reducing SDS-PAGE (15%). Controls without the binding partner are shown for comparison. m, marker; f, flow-through; w, washing step; e1–e3, eluate 1–3.

D. Estimation of the dissociation constant by cross-linking of wild-type enzyme with a constant (left panels) or variable concentration (right panels) of DSS at 37°C. Western blots were quantified as in (B) and the fraction of cross-linked dimer was plotted versus the total protein concentration. The K_d^{app} value determined by non-linear regression was ~5 µM.

potent competitive inhibitor of *P. falciparum* GloI than curcumin because of a more than ten times lower K_i^{app} value and because of the inhibition of both active sites.

We also tested MGFN in parasite cell culture (Fig. 4). Ring stage parasites seemed to be more susceptible to inhibition by MGFN than asynchronous cultures as reflected by IC_{50} values of ~10 and ~20 µM respectively (Fig. 4A). Only late trophozoites and schizonts were found in the asynchronous and in the synchronized ring stage cultures after 48 h treatment with MGFN at concentrations ≥ IC_{50} value (Fig. 4B, upper panels). The remaining cells in the treated cultures tended to have an enlarged food vacuole and to show morphological markers that are typical for dying parasites (Deponte and Becker, 2004). In

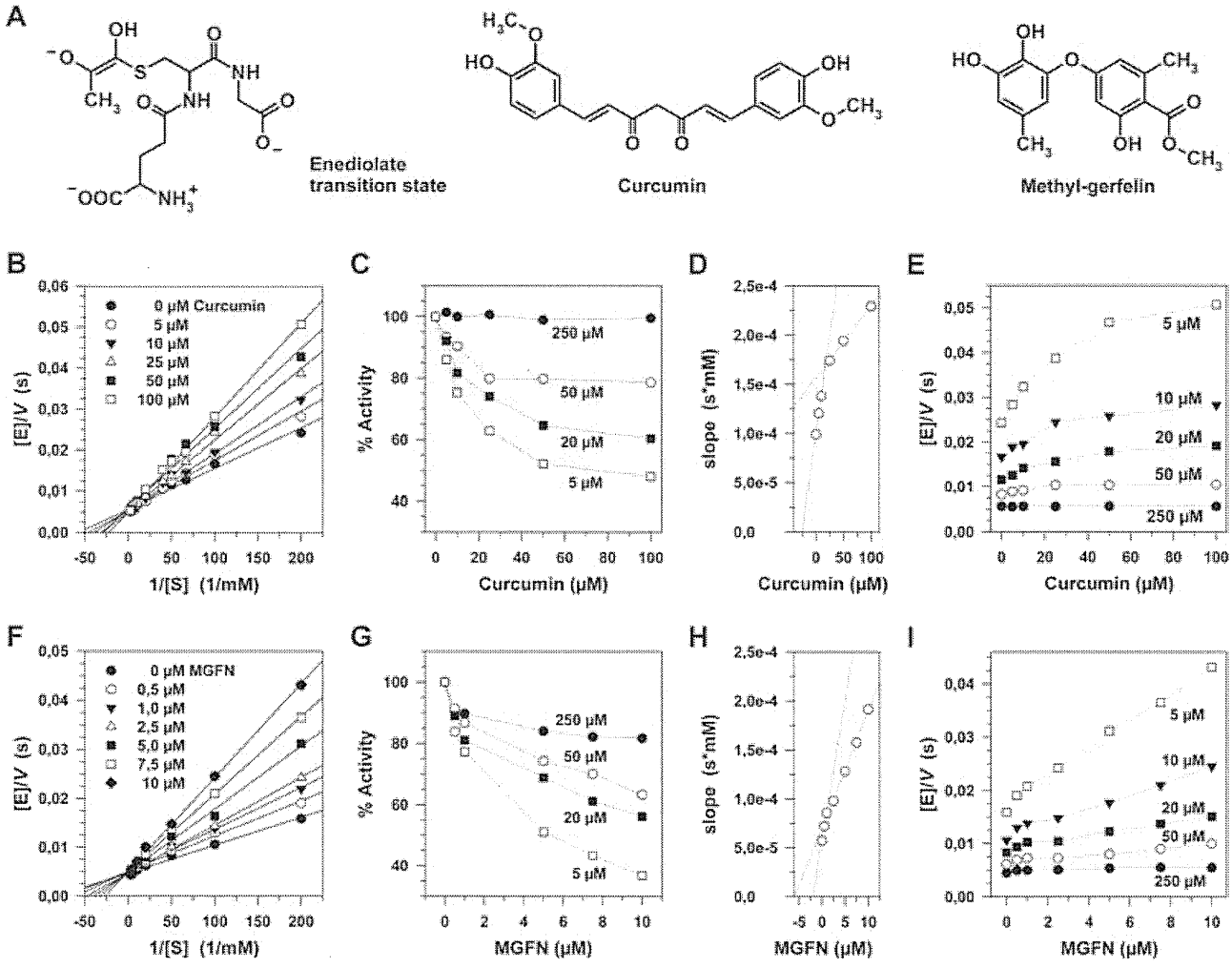

Fig. 3. GloI inhibition studies with curcumin and MGFN *in vitro*.
A. The chemical structures of the GloI glutathionyl-enediolate reaction intermediate, and the inhibitors curcumin and MGFN are shown for comparison.
B.–E. Summarize the steady-state kinetics of GloI with substrate in the presence of 0–100 µM curcumin.
F.–I. Summarize the kinetics with 0–10 µM MGFN. See text and *Experimental procedures* for further details. Data points represent averages from at least three independent transformation/expression/purification experiments.

contrast, the untreated asynchronous control contained approximately 50% ring stages/early trophozoites (Fig. 4B, lower panels) supporting the hypothesis that MGFN had a pronounced effect on ring stage parasites.

Discussion

A functional cytosolic glyoxalase system and the first plastid GloII

Because of the high glycolytic fluxes in malaria parasites, it is not surprising to find a functional glyoxalase system in the cytosol (Fig. 1). In contrast, the physiological function of the apicoplast enzyme tGloII is puzzling. On the one hand, Fleige *et al.* showed that apicoplasts harbour glycolytic isozymes including triosephosphate isomerase (Fleige *et al.*, 2007). Thus, it is likely that methylglyoxal is also formed in these organelles. On the other hand, the second glyoxalase system seems to be incomplete: a functional targeted GloI could not be identified in apicomplexan parasites yet. The hitherto only candidate, the protein GILP form *P. falciparum* (PlasmoDB annotation PFF0230c), was inactive *in vitro*, probably because some active site residues are missing (Akoachere *et al.*, 2005). Accordingly, utilization of other substrates by cGloII cannot be excluded, also because it is well known that glyoxalases II can hydrolyse a variety of thioesters (Uotila, 1973; Wendler *et al.*, 2009). Moreover, even the source of reduced glutathione in the apicoplast is unclear. Is there a targeted glutathione reductase or are there glutathione carriers in the apicoplast?

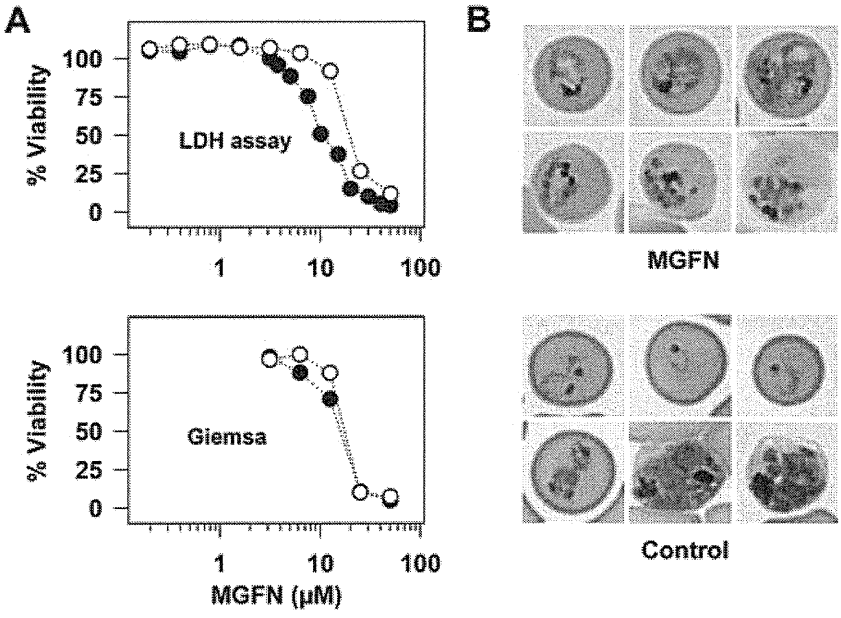

Fig. 4. MGFN inhibition studies in red blood cell cultures.
A. IC_{50} values of ~10 and 20 μM MGFN were determined in an LDH assay using synchronous ring stage parasites (closed circles) and asynchronous parasites (open circles) respectively. Data points from the LDH assay represent averages from triplicate measurements (upper panel). Similar results were obtained by counting 1000–2000 erythrocytes per Giemsa-stained blood smear (lower panel).
B. Representative Giemsa-stained cells from the asynchronous culture treated with 25 μM MGFN and the control. No ring stages were detected in the treated culture after 48 h in contrast to the control.

To our knowledge all non-cytosolic glyoxalases II described so far were found in mitochondria (Bito *et al.*, 1997; Cordell *et al.*, 2004; Marasinghe *et al.*, 2005; Limphong *et al.*, 2009). Thus, despite multiple studied plant isozymes (e.g. in *Arabidopsis thaliana*), tGloII is the first experimentally confirmed plastid GloII. Because of the evolution of the apicoplast (McFadden *et al.*, 1996; Moore *et al.*, 2008) it is quite likely that in the near future further plastid glyoxalases II will be identified in algae and maybe plants.

Uncovering of cGloII dimer formation and potential physiological functions

A monomer–dimer equilibrium (Fig. 2) explains several seemingly contradicting observations of previous studies and point to a physiological relevance of cGloII dimer formation: although glyoxalases II from different organisms were reported to be monomeric (Irsch and Krauth-Siegel, 2004; Marasinghe *et al.*, 2005; Campos-Bermudez *et al.*, 2007), subunit contact sites were observed in the crystal structures of human GloII and mitochondrial Glx2–5 from *A. thaliana* (Cameron *et al.*, 1999; Marasinghe *et al.*, 2005). The two subunits in the crystallized human enzyme had completely accessible active sites and interacted solely along helices α8 and α8′ (including residues Glu^{238}, Arg^{250}, Gln^{254} and Lys^{256} from both subunits) (see PDB entry 1QH5). The dimerization interface of Glx2–5 was much larger and included both substrate-binding sites. Thus, the active sites of crystallized Glx2–5 were not accessible to the substrate (see PDB entry 1XM8). Several of the contact-forming residues of Glx2–5 are conserved in *P. falciparum* cGloII, which might explain why the mutations have altered the monomer–dimer equilibrium (Table 1; Fig. 2A and B).

Could dimer formation also occur *in vivo*? The cellular concentration of GloII from most organisms is unknown. In haploid yeast, having a volume of 30–80 fl (μm^3), ~13 700 molecules of a cytosolic GloII were measured per cell (Ghaemmaghami *et al.*, 2003; http://www.yeastgenome.org/). Dividing the molecules per volume by the Avogadro constant yields a rough estimation of a concentration around 0.3–0.8 μM for yeast GloII. Even if the concentration of cGloII in *P. falciparum* was lower, a K_d^{app} of ~5 μM (Fig. 2D) could be sufficient for partial but significant dimerization: for example, at a protein concentration of 0.1 μM about 4% of cGloII could form a dimer *in vivo*. Such a concentration corresponds to only 1500 molecules of cGloII per *P. falciparum* schizont (having a volume of approximately 30 fl ~ 35 h after red blood cell invasion, Saliba *et al.*, 1998). Obviously, analysing the cellular concentration of *P. falciparum* cGloII and the K_d^{app} of cytosolic yeast GloII is required to quantify dimer formation *in vivo*. What might be the function of a monomer–dimer equilibrium? Kinetic studies on cGloII and its glutathione-binding site mutants did not reveal deviations from typical Michaelis-Menten kinetics (Urscher and Deponte, 2009). Subunit cooperativity during catalysis therefore seems less likely. However, considering that the active site could be completely blocked as observed for crystallized Glx2–5, a regulatory or signalling function because of dimer formation *in vivo* is possible.

Interpretation and misinterpretation of GloI inhibition studies

Inhibition of *P. falciparum* GloI by curcumin and MGFN resulted in complex kinetic patterns (Fig. 3). The *in vitro* formation of curcumin–glutathione conjugates at pH 7.0 is very slow (Awasthi *et al.*, 2000) and did not influence the reaction rates (Fig. S1). Furthermore, inhibition of homodimeric mammalian GloI by curcumin or MGFN resulted in linear Dixon plots (Kawatani *et al.*, 2008; Santel *et al.*, 2008). Thus, the most likely explanation of the complex patterns is that curcumin and MGFN bind with different affinities to the two different active sites of the monomeric enzyme (see also Fig. S2). In addition, inhibitor binding to one reaction centre could alter the conformation and activity of the other active site (Deponte *et al.*, 2007). These mechanistic aspects were overlooked in previous studies on monomeric glyoxalases I. Thus, K_i^{app} values obtained, e.g. for *P. falciparum* GloI (Akoachere *et al.*, 2005) or the commercially available monomeric enzyme from yeast (e.g. Hamilton and Creighton, 1992), have to be interpreted with caution because they represent unweighted averages from different active sites and/or conformations. The true K_i value for one of the active sites could be much higher/lower than the K_i^{app} value depending on: (i) the inhibitor (e.g. Fig. 3B–E vs. Fig. 3F–I), (ii) the way the data were analysed (e.g. Fig. 3D and H vs. Fig. 3E and I), (iii) the range of substrate and inhibitor concentrations tested and (iv) the differences between the active sites.

The IC_{50} value for curcumin in previous *P. falciparum* cell culture experiments was 5 or 25 μM depending on the study (Reddy *et al.*, 2005; Cui *et al.*, 2007). The first/lower K_i^{app} value for GloI with curcumin (Fig. 3D) is in this concentration range. However, this K_i only holds true at low substrate concentrations (Fig. 3C). Inhibition of GloI by curcumin *in vivo* will therefore highly depend on the unknown cellular concentration of the physiological substrate and on whether the targeted active site is required for the turnover of this substrate. Because curcumin is known to have many effects in the micromolar concentration range (e.g. Cui *et al.*, 2007), it seems unlikely that the IC_{50} value in cell culture is solely due to a direct inhibition of GloI. For example, the homodimeric human enzyme was inhibited with a K_i of ~5 μM (Santel *et al.*, 2008), which might be also detrimental for *P. falciparum* in the erythrocyte/parasite unit. MGFN has a similar IC_{50} value in cell culture (Fig. 4) but is a more potent inhibitor of GloI because: (i) it competes with both active sites and (ii) has a more than 10-fold lower K_i^{app} value *in vitro* (Fig. 3H). Both compounds might be a good starting point for drug development of non-glutathione inhibitors because of their similarity with the enediolate transition state. Hydrolysis of the methoxy groups and reducing the size of curcumin (Fig. 3A) might generate a more efficient inhibitor competing with both active sites; a prerequisite that is already met by MGFN.

Experimental procedures

Cloning of GFP- and protein A-tagged glyoxalase constructs

All primers used for the following cloning procedures are given in Table S1. Vectors pHH2 and pARL were a kind gift by Professor A Cowman and colleagues (a summary on the vectors is given in Crabb *et al.*, 2004). The glyoxalase-encoding sequences were identical to accession numbers AF486284, AY494055 and AF486285 (Akoachere *et al.*, 2005). For cloning of constructs encoding C-terminally GFP-tagged full-length glyoxalases the genes *GLOI*, *cGLOII* and *tGLOII* were PCR-amplified using the templates *GLOI*/pQE30 (Deponte *et al.*, 2007), *cGLOII*/pQE30 (Urscher and Deponte, 2009) and *P. falciparum* genomic DNA respectively. PCR products were digested with BamHI and AvrII and cloned into *GFP*/pHH2 using the BglII and AvrII restriction sites. *GFP* fusion constructs were subcloned into pARL-1a with XhoI. Constructs encoding N-terminally protein A-tagged full-length GloI and cGloII without His-tag were cloned as follows. The protein A gene (*pA*) was PCR-amplified and cloned into the NcoI/BamHI restriction sites of pET28a (Novagen) replacing the N-terminal His-tag and the T7-tag. Untagged *GLOI* and *cGLOII* were then subcloned from pQE30 into *pA*/pET28 using BamHI/HindIII and BamHI/SacI, respectively, yielding *pA-GLOI*/pET28 and *pA-cGLOII*/pET28. The orientation and correct sequences of all constructs were confirmed by DNA sequencing both strands.

P. falciparum *cell culture and transfection*

The *P. falciparum* 3D7 line was cultured in human 0^+ erythrocytes according to standard protocols (Trager and Jensen, 1976), except cultures were incubated in gassed flasks. Transfection with the pARL constructs (see above) was carried out by electroporation of infected human 0^+ erythrocytes as previously described (Fidock and Wellems, 1997). GFP-transfectants were selected with 2.5 nM WR99210 (kindly supplied by D Jacobus).

Immunofluorescence assays and live cell imaging

Immunofluorescence assays were carried out following fixation using 4% paraformaldehyde/0.00075% glutaraldehyde as previously described (Tonkin *et al.*, 2004) except fixation was carried out at 37°C for 30 min, and quenching was performed with 125 mM glycine in phosphate-buffered saline (PBS). Primary antibodies used: rabbit anti-ACP (1:500, kindly provided by Professor G McFadden) and anti-rabbit-Cy3 (1:2000, DAKO) were both diluted in 3% BSA/PBS. Hoechst 33258 (Molecular probes) was used in a concentration of 50 ng ml^{-1} for fixed parasites or 10 μg·ml^{-1} for live parasites. All images were acquired at either 37°C (live cells)

or room temperature (fixed cells) on a Zeiss Cell Observer using appropriate filter sets. Individual images were imported into Image J64 (version 1.43b, available at http://rsb.info.nih.gov/ij), converted to eight-bit greyscale, subjected to background subtraction and overlaid. To create figures, TIF files were imported into Powerpoint (Microsoft), assembled and slides exported as TIFs. No gamma adjustments were applied to any image, and all data are presented in accordance with the recommendations of Rossner and Yamada (Rossner and Yamada 2004).

Heterologous expression and protein purification

His-tagged GloI, GloI^{E345Q} and cGloII were expressed in *Escherichia coli* strain XL1-Blue and purified as previously described (Deponte *et al.*, 2007; Urscher and Deponte, 2009). Plasmids *pA-GLOI*/pET28 and *pA-cGLOII*/pET28 were freshly transformed into *E. coli* strain BL21(DE3) (Novagen) before each expression. Bacteria were precultured over night at 37°C in Luria Bertani medium supplemented with 25 mg l^{-1} kanamycin. The preculture was diluted (ratio 1:20) and grown at 37°C to an optical density at 600 nm of 0.3. Then $ZnSO_4$*$7H_2O$ (286 mg l^{-1}) was added and the culture was grown for 30 min before induction with 0.5 mM isopropyl-β-D-1-thiogalactopyranoside. Cells were harvested 4 h after induction by centrifugation (15 min, 4000 *g*, 4°C), washed once and stored at –20°C.

Bacteria expressing protein A-tagged GloI were thawed on ice and resuspended in 5 ml of 10 mM MOPS/NaOH, pH 7.8 per litre of culture. The suspension was stirred for 1 h on ice after addition of lysozyme and DNase I, followed by sonication at 4°C and centrifugation for 30 min at 30 500 *g*, 4°C. The supernatant was applied to an *S*-hexylglutathione agarose column (Sigma), which had been equilibrated with the same buffer. The column was washed with 10 column volumes of 10 mM MOPS/NaOH, 200 mM NaCl, pH 7.8, and recombinant enzyme was eluted with 4.5 column volumes of 10 mM MOPS/NaOH, 200 mM NaCl, 5 mM *S*-hexylglutathione, pH 7.8. *S*-hexylglutathione was subsequently removed by gel filtration chromatography.

Bacteria expressing protein A-tagged cGloII were thawed on ice and resuspended in 5 ml of 50 mM MOPS/NaOH, 300 mM NaCl, 0.05% (v/v) Tween 20, pH 7.8 (MST-buffer) per litre of culture. The suspension was stirred for 1 h on ice after addition of lysoszyme and DNase I, followed by sonication at 4°C and centrifugation for 30 min at 30 500 *g*, 4°C. The supernatant was applied to an IgG-sepharose 6 Fast Flow column (GE Healthcare), which had been equilibrated with MST-buffer. The column was then washed with 10 column volumes of MST-buffer. Afterwards, the column was incubated for 30 min at 4°C with 12 column volumes of 50 mM MOPS, 300 mM NaCl, 125 mM imidazole, pH 7.8 containing an excess of purified His-tagged protein A in order to elute the glyoxalase in a competitive manner. The eluate was diluted 1:10 and applied on a Ni-NTA column (Quiagen) to remove His-tagged protein A. Protein A-tagged cGloII was collected from the flow through and His-tagged protein A was reused after elution with 50 mM MOPS, 300 mM NaCl, 125 mM imidazole, pH 7.8.

Gel filtration chromatography

The apparent molecular mass of the purified proteins was analysed by gel filtration chromatography on a HiLoad 16/60 Superdex 200 prep grade column, which was connected to an ÄKTA-FPLC system (GE Healthcare). The column was calibrated at 4°C with a gel filtration standard (GE Healthcare) and equilibrated with buffer containing 50 mM MOPS/NaOH, 300 mM NaCl, pH 7.2. The same buffer was used for elution. FPLC-fractions were detected photometrically, and peak areas and k_{AV} values were evaluated using the software UNICORN 3.21 (GE Healthcare). Controls with alternative pH values, protein and salt concentrations were performed to validate the obtained results.

Cross-linking experiments

Comparative cross-linking kinetics were carried out with 5–8 μM purified cGloII or cGloII^{R154K} (Urscher and Deponte, 2009) in 50 mM MOPS/NaOH, 300 mM NaCl, 125 mM imidazole, pH 7.8 at 4°C. Equal concentrations of both proteins were incubated in parallel with a 10^3-fold molar excess of glutaraldehyde (Sigma) or a 130-fold molar excess of DSS (Thermo Scientific) in a final volume of 50 μl for the indicated time points. Cross-linking was stopped by adding 5 μl of 1 M Tris-HCl, pH 8.0 to the reaction mixture. After addition of Laemmli-buffer, samples were analysed by reducing 12% SDS-polyacrylamide gel electrophoresis (SDS-PAGE) (Laemmli, 1970) and Western blotting against the N-terminal His-tag using a mouse penta-His primary antibody (Qiagen) and an anti-mouse IgG secondary antibody conjugated with horseradish peroxidase (Bio-Rad). Experiments with glutaraldehyde were repeated twice yielding similar results. Signals from three independent DSS cross-linking/Western blotting experiments were quantified using the software ImageMaster 1D Elite (Amersham Biosciences). The maximum wild-type signal was set to 100%, and results were expressed as a percentage of this signal. The data shown in Fig. 2B were averaged from the three experiments.

In analogy, a K_d^{app} was estimated by cross-linking with DSS. Variable concentrations of purified cGloII were incubated for 10 min at 37°C with a 130-fold molar excess or a constant concentration (130 μM) of DSS in a final volume of 50 μl. A simplified reaction scheme for dimer (*D*) cross-linking with DSS is:

$$2\,M \underset{k_{-1}}{\overset{k_1}{\rightleftharpoons}} D \xrightarrow[DSS]{V_2} D^*$$

Although the exact kinetic law for the formation of the cross-linked dimer (D*) with the velocity V_2 is unknown, and although D* instead of D is measured by SDS-PAGE and western-blotting, an estimation of $K_d = k_{-1}/k_1 = [M]^2/[D]$ is possible (Graziano *et al.*, 2006). The signal intensities for total protein and D* were determined from the blots, and the data were analysed as described in Graziano *et al.* 2006 by non-linear regression analysis using SigmaPlot 10.0 (Systat Software). Additional attempts to confirm the K_d by surface plasmon resonance failed because of unspecific binding of His- and protein A-tagged cGloII to a variety of surfaces.

Pull-down assays with His- and protein A-tagged glyoxalases

Co-purification on IgG-sepharose: frozen bacterial cell pellets containing the His- or protein A-tagged glyoxalases were solubilized in 5 ml of MST-buffer per litre of culture. The suspension was stirred for 1 h on ice after addition of lysozyme and DNase I, followed by sonication at 4°C and centrifugation for 30 min at 30 500 *g*, 4°C. The supernatants with each fusion protein were subsequently mixed, incubated for 10 min on ice and applied to an IgG-sepharose column that had been equilibrated twice with 2–3 column volumes each of 0.5 M acetic acid, pH 3.4, and MST-buffer. The column was then washed with 10 volumes of MST-buffer, followed by a washing step with two volumes of 5 mM ammonium acetate, pH 5.0. The protein A-tagged glyoxalase was eluted with 0.5 M acetic acid, pH 3.4, and the fractions were analysed for co-purified His-tagged protein by reducing 15% SDS-PAGE.

Co-purification on Ni-NTA: frozen bacterial cell pellets containing the His- or protein A-tagged glyoxalases were solubilized in 5 ml of 50 mM MOPS, 300 mM NaCl, 10 mM imidazole, pH 7.8 per litre of culture. The suspension was stirred for 1 h on ice after addition of lysozyme and DNase I, followed by sonication at 4°C and centrifugation for 30 min at 30 500 *g*, 4°C. The supernatants were subsequently mixed, incubated for 10 min on ice and applied to a Ni-NTA column that had been equilibrated with the same buffer. The column was washed with 10 volumes of 50 mM MOPS, 300 mM NaCl, 25 mM imidazole, pH 7.8. The His-tagged protein was eluted with 50 mM MOPS/NaOH, 300 mM NaCl, 125 mM imidazole, pH 7.8, and the fractions were analysed for co-purified protein A-tagged glyoxalase by reducing 15% SDS-PAGE.

MGFN and curcumin inhibition assays

High-performance liquid chromatography-purified curcumin (> 98%) was obtained from Roth. GFN was purified as described previously (Zenitani *et al.*, 2003a,b). Trimethylsilyldiazomethane (2 M) was added to a solution of GFN (0.34 mmol) in methylene chloride (3 ml) and methanol (1 ml), and the mixture was subsequently stirred for 30 min at 0°C. The reaction mixture was extracted with ethyl acetate and washed with brine. The resulting extracts were further purified by reverse-phase high-performance liquid chromatography to yield MGFN as a brown powder.

Enzymatic activity of recombinant GloI was monitored at 30°C using a thermostatted Jasco V-550 UV-visual spectrophotometer (see also Deponte *et al.*, 2007). GloI activity was determined at 240 nm by measuring the conversion of the hemithioacetal (formed between methylglyoxal and GSH) into *S*-D-lactoylglutathione ($\varepsilon_{240\,nm} = 3.37\ mM^{-1}\ cm^{-1}$). Stock solutions of 10 mM GSH (Sigma) and 100 mM methylglyoxal (Sigma) in assay buffer (50 mM MOPS/NaOH pH 7.0), and ≤ 10 mM curcumin and 25 mM MGFN in methanol were freshly prepared before each experiment. For a desired concentration of hemithioacetal, the concentrations of methylglyoxal and GSH in the equilibrated assay mixture were calculated and varied using the equation $K_d = 3\ mM = ([methylglyoxal][GSH]/[hemithioacetal])$. The calculated concentration of free GSH at equilibrium was 0.1 mM in all assays and the calculated initial concentration of the hemithioacetal at equilibrium was 5–500 µM. Accordingly, the concentrations of methylglyoxal and GSH before equilibration were 0.155–15.5 mM and 0.105–0.6 mM respectively. The hemithioacetal was formed during a preincubation period of 5 min at 30°C (longer preincubation for 10 min led to very similar reaction rates). The inhibitor was added after 4 min during the 5 min preincubation period, and the reaction was initiated by the addition of enzyme (5 nM in all assays). The highest final concentration of methanol in the assay was 1% for curcumin and 0.5% for MGFN. Controls confirmed that the activity of GloI was not significantly affected by methanol under the chosen assay conditions.

Inhibition of parasite growth by MGFN was determined by counting Giemsa-stained blood smears and by a photometric lactate dehydrogenase (LDH) assay as previously described (Makler *et al.*, 1993). MGFN (20 mM, dissolved in methanol) was diluted stepwise in the cell culture medium. Afterwards, asynchronous parasite cultures or synchronized ring stage parasite cultures were added to the medium resulting in a final MGFN concentration of 0.05–100 µM (0.0002–0.5% methanol). Cultures were grown for 48 h before preparation of blood smears and for 72 h before readout of the LDH assay. Pictures of Giemsa-stained parasites were taken on a Zeiss Axiovert 200 and assembled in CorelDraw 12. The overall brightness and contrast of the whole image was adjusted in order to highlight the Giemsa-stained parasites. Results from the LDH assay were corrected for background (erythrocytes only) and the data from mock treated parasite cultures (containing the corresponding concentration of methanol) were set to 100%. Results were expressed as a percentage of the mock treated control.

Acknowledgements

This work was supported by the Deutsche Forschungsgemeinschaft (DFG) grant De1431/1 and in part by a travel allowance of the Boehringer Ingelheim fonds (to MD). JMP is supported by the DFG collaborative research centre (SFB) TR1. We wish to thank Stephan Uebel for analytical ultracentrifugation, Nadja Braun for help with the LDH assays and Petra Heckmeyer for her excellent technical assistance. MD is especially grateful to Professor Alan Cowman and colleagues for support and discussions during a vocational training at the Walter and Eliza Hall Institute.

References

Aggarwal, B.B., and Sung, B. (2009) Pharmacological basis for the role of curcumin in chronic diseases: an age-old spice with modern targets. *Trends Pharmacol Sci* **30:** 85–94.

Akoachere, M., Iozef, R., Rahlfs, S., Deponte, M., Mannervik, B., Creighton, D.J., *et al.* (2005) Characterization of the glyoxalases of the malarial parasite *Plasmodium falciparum* and comparison with their human counterparts. *Biol Chem* **386:** 41–52.

Awasthi, S., Pandya, U., Singhal, S.S., Lin, J.T., Thiviyanathan, V., Seifert, W.E., *et al.* (2000) Curcumin-

glutathione interactions and the role of human glutathione *S*-transferase P1-1. *Chem Biol Interact* **128:** 19–38.

Bito, A., Haider, M., Hadler, I., and Breitenbach, M. (1997) Identification and phenotypic analysis of two glyoxalase II encoding genes from *Saccharomyces cerevisiae*, GLO2 and GLO4, and intracellular localization of the corresponding proteins. *J Biol Chem* **272:** 21509–21519.

Cameron, A.D., Ridderström, M., Olin, B., and Mannervik, B. (1999) Crystal structure of human glyoxalase II and its complex with a glutathione thiolester substrate analogue. *Structure* **7:** 1067–1078.

Campos-Bermudez, V.A., Leite, N.R., Krog, R., Costa-Filho, A.J., Soncini, F.C., Oliva, G., and Vila, A.J. (2007) Biochemical and structural characterization of *Salmonella typhimurium* glyoxalase II: new insights into metal ion selectivity. *Biochemistry* **46:** 11069–11079.

Cordell, P.A., Futers, T.S., Grant, P.J., and Pease, R.J. (2004) The human hydroxyacylglutathione hydrolase (HAGH) gene encodes both cytosolic and mitochondrial forms of glyoxalase II. *J Biol Chem* **279:** 28653–28661.

Crabb, B.S., Rug, M., Gilberger, T.W., Thompson, J.K., Triglia, T., Maier, A.G., and Cowman, A.F. (2004) Transfection of the human malaria parasite *Plasmodium falciparum*. *Methods Mol Biol* **270:** 263–276.

Cui, L., Miao, J., and Cui, L. (2007) Cytotoxic effect of curcumin on malaria parasite *Plasmodium falciparum*: inhibition of histone acetylation and generation of reactive oxygen species. *Antimicrob Agents Chemother* **51:** 488–494.

Deponte, M., and Becker, K. (2004) *Plasmodium falciparum* – do killers commit suicide? *Trends Parasitol* **20:** 165–169.

Deponte, M., and Becker, K. (2005) Biochemical characterization of *Toxoplasma gondii* 1-Cys peroxiredoxin 2 with mechanistic similarities to typical 2-Cys Prx. *Mol Biochem Parasitol* **140:** 87–96.

Deponte, M., Sturm, N., Mittler, S., Harner, M., Mack, H., and Becker, K. (2007) Allosteric coupling of two different functional active sites in monomeric *Plasmodium falciparum* glyoxalase I. *J Biol Chem* **282:** 28419–28430.

Fidock, D.A., and Wellems, T.E. (1997) Transformation with human dihydrofolate reductase renders malaria parasites insensitive to WR99210 but does not affect the intrinsic activity of proguanil. *Proc Natl Acad Sci USA* **94:** 10931–10936.

Fleige, T., Fischer, K., Ferguson, D.J., Gross, U., and Bohne, W. (2007) Carbohydrate metabolism in the *Toxoplasma gondii* apicoplast: localization of three glycolytic isoenzymes, the single pyruvate dehydrogenase complex, and a plastid phosphate translocator. *Eukaryot Cell* **6:** 984–996.

Ghaemmaghami, S., Huh, W.K., Bower, K., Howson, R.W., Belle, A., Dephoure, N., *et al.* (2003) Global analysis of protein expression in yeast. *Nature* **425:** 737–741.

Graziano, V., McGrath, W.J., Yang, L., and Mangel, W.F. (2006) SARS CoV main proteinase: the monomer-dimer equilibrium dissociation constant. *Biochemistry* **45:** 14632–14641.

Hamilton, D.S., and Creighton, D.J. (1992) Inhibition of glyoxalase I by the enediol mimic S-(N-hydroxy-N-methylcarbamoyl)glutathione. The possible basis of a tumor-selective anticancer strategy. *J Biol Chem* **267:** 24933–24936.

Iozef, R., Rahlfs, S., Chang, T., Schirmer, H., and Becker, K. (2003) Glyoxalase I of the malarial parasite *Plasmodium falciparum*: evidence for subunit fusion. *FEBS Lett* **554:** 284–288.

Irsch, T., and Krauth-Siegel, R.L. (2004) Glyoxalase II of African trypanosomes is trypanothione-dependent. *J Biol Chem* **279:** 22209–22217.

Kawatani, M., Okumura, H., Honda, K., Kanoh, N., Muroi, M., Dohmae, N., *et al.* (2008) The identification of an osteoclastogenesis inhibitor through the inhibition of glyoxalase I. *Proc Natl Acad Sci USA* **105:** 11691–11696.

Laemmli, U.K. (1970) Cleavage of structural proteins during the assembly of the head of bacteriophage T4. *Nature* **227:** 680–685.

Limphong, P., Nimako, G., Thomas, P.W., Fast, W., Makaroff, C.A., and Crowder, M.W. (2009) *Arabidopsis thaliana* mitochondrial glyoxalase 2-1 exhibits beta-lactamase activity. *Biochemistry* **48:** 8491–8493.

McFadden, G.I., Reith, M.E., Munholland, J., and Lang-Unnasch, N. (1996) Plastid in human parasites. *Nature* **381:** 482.

Makler, M.T., Ries, J.M., Williams, J.A., Bancroft, J.E., Piper, R.C., Gibbins, B.L., and Hinrichs, D.J. (1993) Parasite lactate dehydrogenase as an assay for *Plasmodium falciparum* drug sensitivity. *Am J Trop Med Hyg* **48:** 739–741.

Marasinghe, G.P., Sander, I.M., Bennett, B., Periyannan, G., Yang, K.W., Makaroff, C.A., and Crowder, M.W. (2005) Structural studies on a mitochondrial glyoxalase II. *J Biol Chem* **280:** 40668–40675.

Moore, R.B., Oborník, M., Janouskovec, J., Chrudimský, T., Vancová, M., Green, D.H., *et al.* (2008) A photosynthetic alveolate closely related to apicomplexan parasites. *Nature* **451:** 959–963.

Nandakumar, D.N., Nagaraj, V.A., Vathsala, P.G., Rangarajan, P., and Padmanaban, G. (2006) Curcumin-artemisinin combination therapy for malaria. *Antimicrob Agents Chemother* **50:** 1859–1860.

Nickel, C., Rahlfs, S., Deponte, M., Koncarevic, S., and Becker, K. (2006) Thioredoxin networks in the malarial parasite *Plasmodium falciparum*. *Antioxid Redox Signal* **8:** 1227–1239.

Reddy, R.C., Vatsala, P.G., Keshamouni, V.G., Padmanaban, G., and Rangarajan, P.N. (2005) Curcumin for malaria therapy. *Biochem Biophys Res Commun* **326:** 472–474.

Rossner, M., and Yamada, K.M. (2004) What's in a picture? The temptation of image manipulation. *J Cell Biol* **166:** 11–15.

Saliba, K.J., Horner, H.A., and Kirk, K. (1998) Transport and metabolism of the essential vitamin pantothenic acid in human erythrocytes infected with the malaria parasite *Plasmodium falciparum*. *J Biol Chem* **273:** 10190–10195.

Santel, T., Pflug, G., Hemdan, N.Y., Schäfer, A., Hollenbach, M., Buchold, M., *et al.* (2008) Curcumin inhibits glyoxalase 1: a possible link to its anti-inflammatory and anti-tumor activity. *PLoS One* **3:** e3508.

Segel, I.H. (1993) *Enzyme Kinetics: Behavior and Analysis of Rapid Equilibrium and Steady State Enzyme Systems*. New York: John Wiley and Sons.

Sherman, I.W. (1979) Biochemistry of *Plasmodium* (malarial parasites). *Microbiol Rev* **43:** 453–495.

Thornalley, P.J. (1990) The glyoxalase system: new develop-

ments towards functional characterization of a metabolic pathway fundamental to biological life. *Biochem J* **269:** 1–11.

Thornalley, P.J. (1996) Pharmacology of methylglyoxal: formation, modification of proteins and nucleic acids, and enzymatic detoxification – a role in pathogenesis and antiproliferative chemotherapy. *Gen Pharmacol* **27:** 565–573.

Thornalley, P.J., Strath, M., and Wilson, R.J.M. (1994) Antimalarial activity *in vitro* of the glyoxalase I inhibitor diester, *S*-p-bromobenzylglutathione diethyl ester. *Biochem Pharmacol* **47:** 418–420.

Tonkin, C.J., van Dooren, G.G., Spurck, T.P., Struck, N.S., Good, R.T., Handman, E., *et al.* (2004) Localization of organellar proteins in *Plasmodium falciparum* using a novel set of transfection vectors and a new immunofluorescence fixation method. *Mol Biochem Parasitol* **137:** 13–21.

Trager, W., and Jensen, J.B. (1976) Human malaria parasites in continuous culture. *Science* **193:** 673–675.

Uotila, L. (1973) Purification and characterization of *S*-2-hydroxyacylglutathione hydrolase (glyoxalase II) from human liver. *Biochemistry* **12:** 3944–3951.

Urscher, M., and Deponte, M. (2009) *Plasmodium falciparum* glyoxalase II: Theorell-Chance product inhibition patterns, rate-limiting substrate binding via Arg^{257}/Lys^{260}, and unmasking of acid-base catalysis. *Biol Chem* **390:** 1171–1183.

Vander Jagt, D.L., Hunsaker, L.A., Campos, N.M., and Baack, B.R. (1990) d-lactate production in erythrocytes infected with *Plasmodium falciparum. Mol Biochem Parasitol* **42:** 277–284.

Waller, R.F., Reed, M.B., Cowman, A.F., and McFadden, G.I. (2000) Protein trafficking to the plastid of *Plasmodium falciparum* is via the secretory pathway. *EMBO J* **19:** 1794–1802.

Wendler, A., Irsch, T., Rabbani, N., Thornalley, P.J., and Krauth-Siegel, R.L. (2009) Glyoxalase II does not support methylglyoxal detoxification but serves as a general trypanothione thioesterase in African trypanosomes. *Mol Biochem Parasitol* **163:** 19–27.

Zenitani, S., Tashiro, S., Shindo, K., Nagai, K., Suzuki, K., and Imoto, M. (2003a) Gerfelin, a novel inhibitor of geranylgeranyl diphosphate synthase from *Beauveria felina* QN22047. I. Taxonomy, fermentation, isolation, and biological activities. *J Antibiot* **56:** 617–621.

Zenitani, S., Shindo, K., Tashiro, S., Sekiguchi, M., Nishimori, M., Suzuki, K., and Imoto, M. (2003b) Gerfelin, a novel inhibitor of geranylgeranyl diphosphate synthase from *Beauveria felina* QN22047. II. Structural elucidation. *J Antibiot* **56:** 658–660.

Zuegge, J., Ralph, S., Schmuker, M., McFadden, G.I., and Schneider, G. (2001) Deciphering apicoplast targeting signals – feature extraction from nuclear-encoded precursors of *Plasmodium falciparum* apicoplast proteins. *Gene* **280:** 19–26.

Supporting information

Additional supporting information may be found in the online version of this article.

Please note: Wiley-Blackwell are not responsible for the content or functionality of any supporting materials supplied by the authors. Any queries (other than missing material) should be directed to the corresponding author for the article.

DEVELOPMENTAL DYNAMICS 239:818–827, 2010

RESEARCH ARTICLE

Mesenchyme Cells Can Function to Induce Epithelial Cell Proliferation in Starfish Embryos

Gen Hamanaka,[1,2] Midori Matsumoto,[1] Masaya Imoto,[1] and Hiroyuki Kaneko[2]*

Here, we show that mesenchyme cells have a novel morphogenetic function in epithelial cell proliferation in starfish embryos. Blastula embryos were injected with pure populations of mesenchyme cells and the total cell numbers in the treated embryos were subsequently determined at different developmental stages. When a total of 40–50 mesenchyme cells was injected, total cells numbers in mid-gastrula embryos and 3-day-old bipinnaria larvae increased significantly (by 1.3-fold) compared with controls, with no indication of any mitotic activity in the injected mesenchyme cells. However, injection of more than 150 mesenchyme cells failed to induce proliferation of the epithelial cells and, moreover, interfered with normal morphogenesis. These developmental abnormalities occurred concomitantly with a severe condensation of the fibrous component of the extracellular matrix. Our data suggest that epithelial cell proliferation is induced by an appropriate number of mesenchyme cells in concert with the fibrous component of the extracellular matrix. *Developmental Dynamics 239:818–827, 2010.* © 2010 Wiley-Liss, Inc.

Key words: mesenchyme cells; epithelial cells; starfish embryo; proliferation; induction; injection; cytometric analysis

Accepted 3 December 2009

INTRODUCTION

During morphogenesis in triploblastic animals, some cell types in the embryos perform a range of functions involving a variety of different cell behaviors. Identification of the range of functions performed by each cell type will be essential for a more complete understanding of how embryonic cells interact to achieve normal development (Wood and Jacinto, 2007). In starfish embryos, mesenchyme cells contribute to embryonic morphogenesis in at least two distinct ways. First, mesenchyme cells can control some components of the extracellular matrix (ECM). For example, they guide the basal lamina from the tip of the archenteron to the ectodermal stomodeum during mouth formation (Crawford and Abed, 1983; Abed and Crawford, 1986). Mesenchyme cells also exert mechanical tension against the fibrous component of the ECM to sustain embryonic and larval shape (Crawford, 1990; Crawford et al., 1997; Kaneko et al., 2005). Second, mesenchyme cells act as scavengers to clean out the blastocoel. The mesenchyme cells phagocytose cell debris dispersed in the blastocoel during reconstruction of gastrula embryos, thereby allowing morphogenesis to proceed (Tamura et al., 1998). The scavenger function of mesenchyme cells is also essential in normal bipinnaria larva for keeping the blastocoelic environment clean, in particular to deal with dying epithelial cells that fall into the blastocoel and with any unexpected foreign bodies that have invaded through the ectodermal wall (Furukawa et al., 2009). Thus, mesenchyme cells are multifunctional cells that support several aspects of starfish morphogenesis.

In some species of starfish, morphogenesis is achieved by a simple structural change in the epithelial monolayer that comprises the bulk of the

Additional Supporting Information may be found in the online version of this article.

[1]School of Fundamental Science and Technology, Graduate School of Science and Technology, Keio University, Kohoku-ku, Yokohama, Japan
[2]Department of Biology, Research and Education Center for Natural Sciences, Keio University, Kohoku-ku, Yokohama, Japan
***Correspondence to: Hiroyuki Kaneko, Department of Biology, Research and Education Center for Natural Sciences, Keio University, 4-1-1 Hiyoshi, Kohoku-ku, Yokohama, 223-8521, Japan. E-mail: theband@hc.cc.keio.ac.jp**

DOI 10.1002/dvdy.22211
Published online 8 January 2010 in Wiley InterScience (www.interscience.wiley.com).

© 2010 Wiley-Liss, Inc.

Developmental Dynamics

embryonic and larval body (Kuraishi and Osanai, 1992). During the blastula stage, the epithelial layer forms a hollow sphere-like structure as a monolayer of cells. By the mid-gastrula stage, invagination of the vegetal portion of the epithelial monolayer occurs to initiate archenteron formation. In the mid-gastrula stage, the mesenchyme cells ingress into the blastocoel from the tip of the archenteron, and then disperse to the ectoderm and endoderm epithelial walls (Dan-Sohkawa et al., 1980). By the bipinnaria stage, the embryo has enlarged and successively formed several organs while preserving the epithelial monolayer throughout its body. With the exception of a transient period when a small number of muscle progenitor cells emerge from coelomic pouches (Crawford and Chia, 1978), mesenchyme cells are the only cells within the blastocoel. In 4-day-old bipinnaria larvae, mesenchyme cell numbers range from 150 to 190, approximately 1% of the total cell number in the larval body (Furukawa et al., 2009). Throughout this developmental period, the transparency of the embryonic and larval body of starfish allows visualization of the wide range of mesenchyme cell behaviors (Crawford and Chia, 1978; Dan-Sohkawa et al., 1980; Kaneko et al., 1990, 1995b; Kuraishi and Osanai, 1992).

One approach to identification of novel morphogenetic functions of mesenchyme cells is to exploit in vivo situations in which the embryonic body is comprised only of epithelial cells as the mesenchyme cells have yet to appear in the blastocoel. Comparison of the patterns of embryonic development in the presence or absence of mesenchyme cells will shed light upon possible novel functions of the mesenchyme cells. We previously developed an in vitro culture system in which a pure population of mesenchyme cells can be prepared for injection into the blastocoel of a blastula embryo (Kaneko et al., 1995a,b, 2005; Furukawa et al., 2009). Interestingly, in preliminary experiments using a variety of mesenchyme cell numbers, several of the blastula embryos grew larger than normal by the late gastrula and/or bipinnaria stages (see also Fig. 6). This finding indicates the possibility that mesenchyme cells induce epithelial cells to proliferate, resulting in the larger phenotype.

The purpose of this study was to determine whether mesenchyme cells have a function in inducing epithelial cells to proliferate and, to this end, we used our mesenchyme cell injection approach with blastula embryos of the starfish *Asterina pectinifera*. We also used a bacteria counter to assess total cell numbers in individual embryos and larvae. Our cytometric analyses and immunohistochemical observation of 5-bromo-2′-deoxyuridine (BrdU)-treated specimens showed that injection of mesenchyme cells could stimulate a significant increase in epithelial cell numbers. However, at the largest number of injected cells, we observed a lack of effect on epithelial cell proliferation and also morphogenetic abnormalities in the embryos. This response was associated with a severe condensation of the fibrous component of the extracellular matrix. We propose that epithelial cell proliferation in the starfish embryo requires the presence of an appropriately sized population of mesenchyme cells and also responds to the interaction of mesenchyme cells and the fibrous component of the extracellular matrix.

RESULTS

Blastula Embryos Show Proliferation of Epithelial Cells as They Develop to the Mid-gastrula Stage

The structures of blastula and mid-gastrula embryos were assessed with regard to the distributions of their constituent cell types (see the Experimental Procedures section). Blastula embryos were composed of a monolayer of epithelial cells and had a hollow sphere-like appearance (Fig. 1A,B). The epithelial cells retained this monolayer structure until the mid-gastrula stage (Fig. 1C,D). The blastula embryos formed an archenteron (endoderm) as they enlarged along the anteroposterior axis (Fig. 1C,D). Up to the mid-gastrula stage, no mesenchyme cells were present in the blastocoel. Cytometric analysis of 3 combined samples of 30 embryos yielded an average of 3,325.9 (SD ± 384.3) cells in each blastula embryo and of 4,744 (SD ± 384.1) cells in each mid-gastrula embryo. From the blastula to mid-gastrula stages, TUNEL (terminal deoxynucleotidyl transferase–mediated deoxyuridinetriphosphate nick end-labeling; Supp. Fig. S1, which is available online) and propidium iodide (PI) assays (data not shown) detected a small amount of apoptosis but no necrotic signals, respectively (Supp. Fig. S1).

Each Blastula Embryo Is Composed of 3,000–3,500 Cells

Blastula embryos from any given batch showed some variation in size, although they all appeared to have a similar, hollow sphere-like structure (Fig. 2A–F). We attempted to approximate the size of individual blastula embryos by calculating the volume occupied by the epithelial cells around the hollow sphere: the longest (R, r) and shortest axes (R′, r′) of both the outer and inner diameters of the sphere were measured (see Fig. 2G); (R+R′)/2 and (r+r′)/2 were defined as the outer diameter and inner diameters, respectively. Using the bacteria counter, the numbers of cells were separately determined for six blastula embryos in four independent experiments; total cell numbers were plotted against the estimated volume of each blastula embryo (Fig. 2H). Regardless of the significant differences in estimated volumes, the total cell numbers ranged only between 3,000 and 3,500. The plotted data in Figure 2H clearly demonstrate the absence of any relationship between total cell numbers and estimated volumes of the embryos; this is illustrated by comparison of the embryos labeled "a" and "c," which have similar total cell numbers but differ widely in estimated volumes. The total cell numbers per embryo obtained using the bacteria counter are very similar to those estimated from the combined sample of 30 embryos (see also Supp. Table S1).

Injection of Mesenchyme Cells Into Blastula Embryos Increases Total Cell Numbers at the Mid-gastrula Stage

Because the bacteria counter produced a robust estimate of the total cell

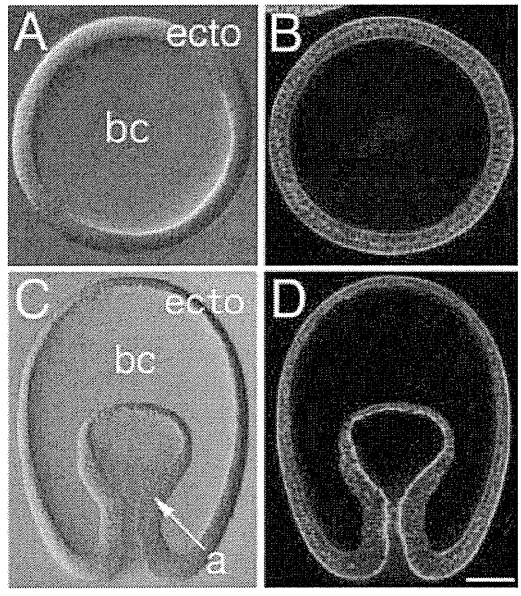

Fig. 1.

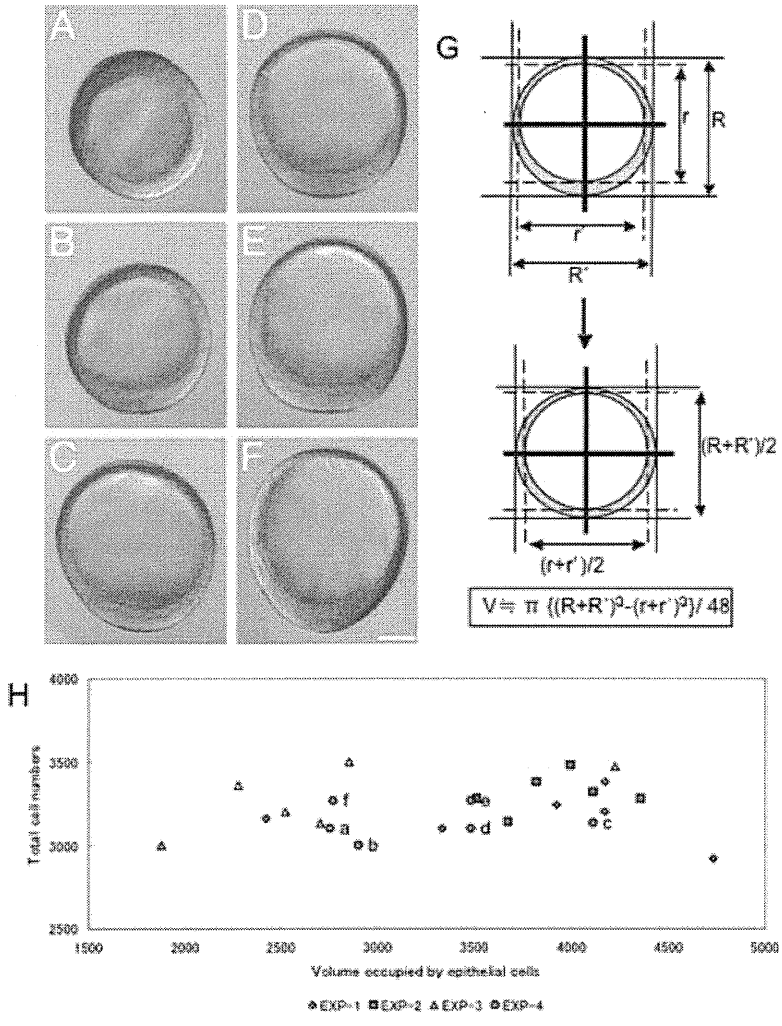

Fig. 2.

numbers in individual embryos, we used this method to address the question of whether mesenchyme cells have a morphogenetic function as an inducer of epithelial cell proliferation. Blastula embryos were injected with 40–50 cultured mesenchyme cells and allowed to develop until the mid-gastrula stage, at which time cytometric analysis was carried out (Figs. 3, 4). Control embryos were injected with similar numbers of ectodermal epithelial cells prepared from late-gastrula embryos; here, we term these cells "epithelial cells." Immediately after injection, the mesenchyme or epithelial cells remained as an aggregate in the blastocoel (Fig. 3A,C). When blastula embryos injected with mesenchyme cells reached the mid-gastrula stage, the mesenchyme cells had separated and were dispersed beneath the epithelial cells of the ectodermal and endodermal wall (Fig. 3B). We found that the mesenchyme cell aggregates consisted of between 40 and 50 cells, based on embryos in which the cells had dispersed (Fig. 3B). In contrast, injected epithelial cells stayed in the aggregates in recipient embryos during the corresponding developmental

Fig. 1. Structure of blastula (**A,B**) and mid-gastrula embryos (**C,D**) of the starfish *Asterina pectinifera*. Blastula embryos reach the mid-gastrula stage after 8 hr at 20°C. A–D: Paired Nomarski (A,C) and fluorescence (B,D) images of paraformaldehyde (PFA)-fixed embryos optically sectioned at the median plane. Both blastula and mid-gastrula embryos are characterized by the presence of an epithelial monolayer and the lack of mesenchyme cells in the blastocoel. In B and C, cell boundaries and the positions of nuclei in epithelial cells were identified after staining with phalloidin (green) and propidium iodide (red), respectively. bc, blastocoel; a, archenteron (endoderm); ecto, ectoderm. Scale bar = 50 μm.

Fig. 2. Total cell numbers in individual blastula embryos. **A–F**: Nomarski microscopic images of live blastula embryos optically sectioned at the median plane. The embryos differ in size. **G**: Outline of the method used to approximate the size of a hollow sphere structure and the formula for calculating the volume occupied by the epithelial monolayer. **H**: Graph showing total cell numbers of individual blastula embryos plotted against their volume as calculated in G. Green dots with lower-case letters correspond to the embryos shown in A to F. Six embryos were tested in four independent batches. Scale bar = 50 μm.

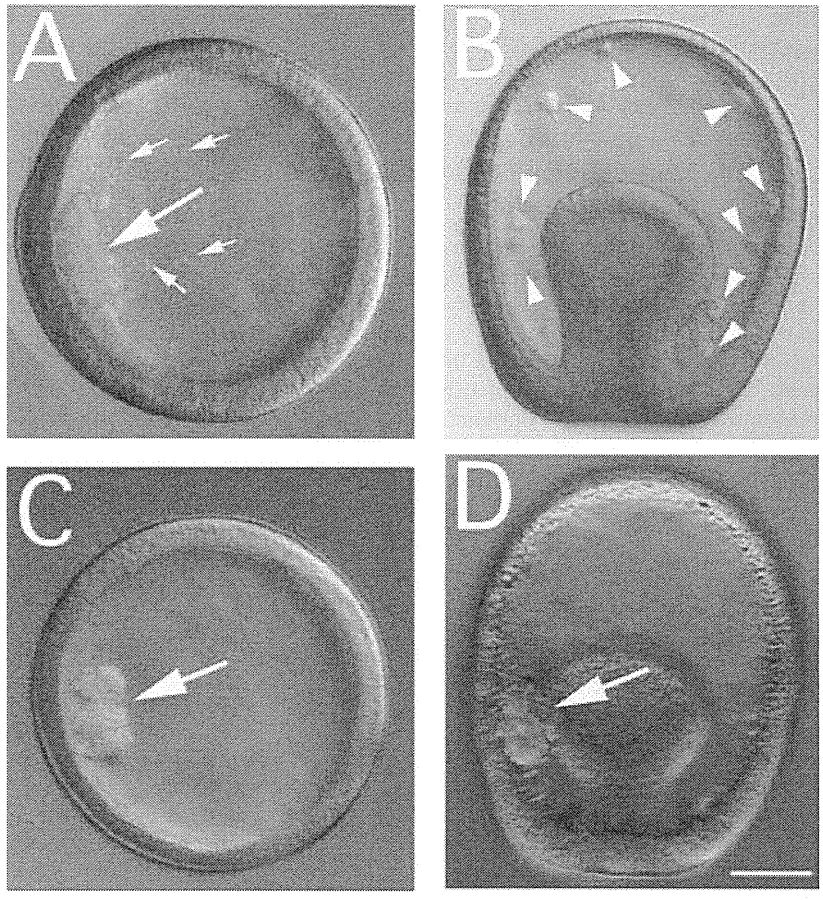

Fig. 3.

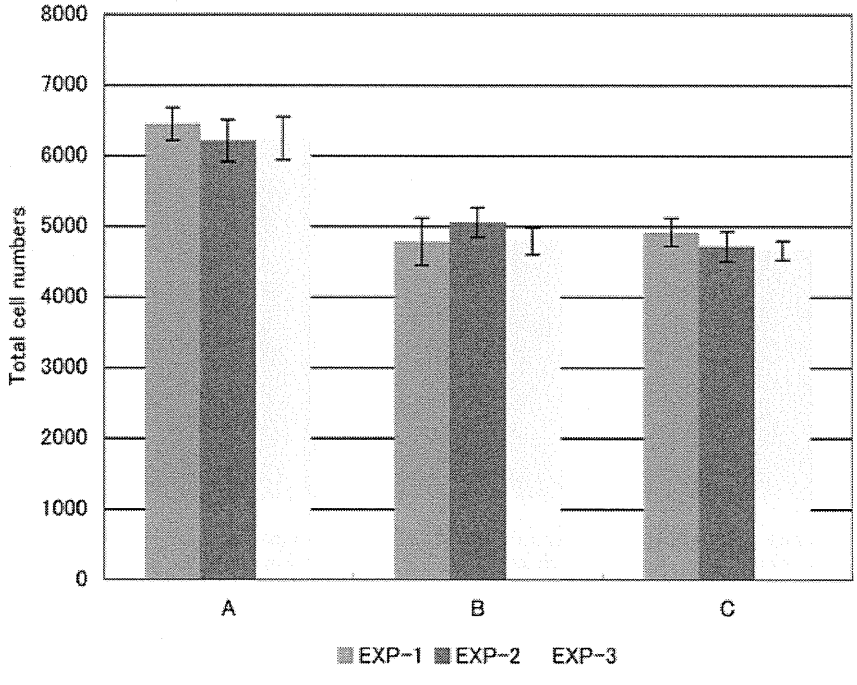

Fig. 4.

period (Fig. 3D). These aggregates also appeared to contain between 40 and 50 cells based on analyses of paraformaldehyde (PFA)-fixed samples that had been stained with PI (Supp. Fig. S2). Sham-injected embryos, an additional control experiment, developed normally to the mid-gastrula stage (data not shown). There were no differences in apparent size and shape of the mid-gastrula embryos in the three experimental groups.

Between five and eight mid-gastrula embryos, similar to those depicted in Figure 3, were prepared for cytometric analyses from each experimental group (Fig. 4). We found that the embryos injected with mesenchyme cells had a significant increase in the total number of cells (approximately 1.3-fold) compared with those in two control experiments (Fig. 4, Supp. Table S1). The total cell numbers of mid-gastrula embryos in the two control experiments were similar to those obtained in our earlier analysis of the combined sample of thirty mid-gastrula embryos allowed to develop normally (see Supp. Table S1).

Fig. 3. Injection experiments with mesenchyme cells (**A,B**) or epithelial cells (**C,D**) in blastula embryos. A,C: Embryos immediately after injection. The 40–50 injected mesenchyme or epithelial cells form a similarly sized aggregate (large arrows) that is clearly different from cell debris (A, small arrows). B,D: Embryos 8 hr after injection. All panels show Nomarski microscopic images merged with fluorescent images of live embryos optically sectioned at the median plane. The injected samples indicated by B and D are at the mid-gastrula stage. The mesenchyme cells have dispersed throughout the blastocoel (arrowheads in B), whereas the epithelial cells remain in an aggregate (arrow in D). The number of injected mesenchyme cells was determined to be between 40 and 50 cells by analyzing all the optical sections of each embryo. Scale bar = 50 μm.

Fig. 4. Effect of injection of mesenchyme cells into blastula embryos on total cell numbers at the mid-gastrula stage. **A–C**: The data are displayed as follows: mesenchyme cells injected (A), epithelial cells injected (B), no cells injected (sham control; C). The numbers of injected mesenchyme cells and epithelial cells were almost identical, as shown in Figure 3. In three independent experiments, the total cell numbers shown represent the average of five to eight individual embryos (with standard deviations; bars). Notably, there was a significant increase in total cell numbers at the mid-gastrula stage following injection of mesenchyme cells into blastula embryos (A).

Injected Mesenchyme Cells Do Not Show Mitotic Activity in the Blastocoel of Recipient Embryos

To determine whether proliferation of the injected mesenchyme cells contributed to the increase in total cell number, we cultured some blastula embryos in artificial seawater containing BrdU. These embryos were then examined under the laser confocal microscope (Fig. 5). BrdU-positive signals were detected in almost all epithelial cells of the ectodermal and endodermal wall but not in mesenchyme cells (Fig. 5A,B). Optical sections of mesenchyme cells at a higher magnification confirmed that there was no indication of BrdU staining in these cells (Fig. 5C).

Effect of Injection With an Excess Number of Mesenchyme Cells on Later Morphogenesis

To examine whether varying the numbers of injected mesenchyme cells influenced later morphogenesis in recipient embryos, we compared development in embryos injected at the blastula stage with either the equivalent number of mesenchyme cells as in the experiments described above or with approximately three to four times that number. The injected embryos were allowed to develop to the 3-day-old bipinnaria stage. Examination of embryos with dispersed rhodamine B isothiocyanate-celite (RITC)-labeled mesenchyme cells after two days of development indicated that the two embryo treatment groups received approximately 40–50 or 150–200 cells, respectively (Fig. 6A,B,D,E). The injected mesenchyme cells were dispersed as single cells (Fig. 6C,F) and coexisted with the innate mesenchyme cells (see also Supp. Fig. S3). In the description below, we refer to these different quantities of injected mesenchyme cells as moderate or excess, respectively. A sham injection group was used as the control. Blastula embryos injected with the moderate number of mesenchyme cells showed normal morphogenetic development, except for size, compared with embryos in the sham control group at the late-gastrula and bipinnaria stages (Fig. 6B,C,H,I). In contrast, blastula embryos injected with the excess number of mesenchyme cells showed significantly altered development with some morphological abnormalities, e.g., the tip of the archenteron and the anterior portion of the ectodermal wall failed to bulge and constrict, respectively, 2 days after injection (Fig. 6E). Subsequently, further skewed morphogenesis resulted in 3-day-old bipinnaria larvae with abnormal morphologies, although the mouth, esophagus, stomach, intestine, coelomic pouches and ciliary bands did form (Fig. 6F). These larvae appeared

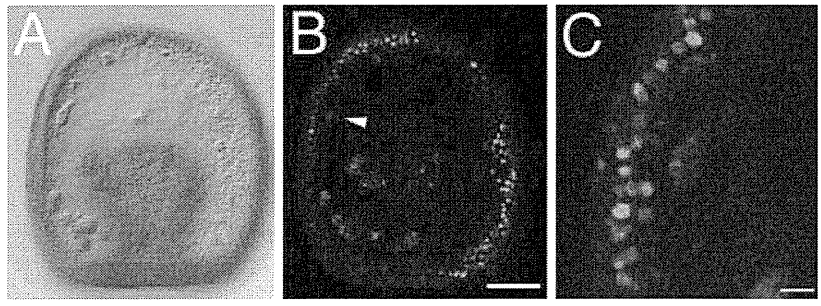

Fig. 5. 5-bromo-2′-deoxyuridine (BrdU) treatment experiment. **A**: Nomarski microscopic image of an embryo fixed with paraformaldehyde (PFA) at the mid-gastrula stage following injection of mesenchyme cells at the blastula stage. The image shows an optical section at the median plane. **B**: Fluorescent image of the embryo shown in (A). BrdU-positive signals (green) were only observed in epithelial cells and not in the injected mesenchyme cells (red). **C**: Higher magnification stack of images from eleven optical sections from the position indicated by the arrowhead in B. Scale bars = 50 μm in A,B; 10 μm in C.

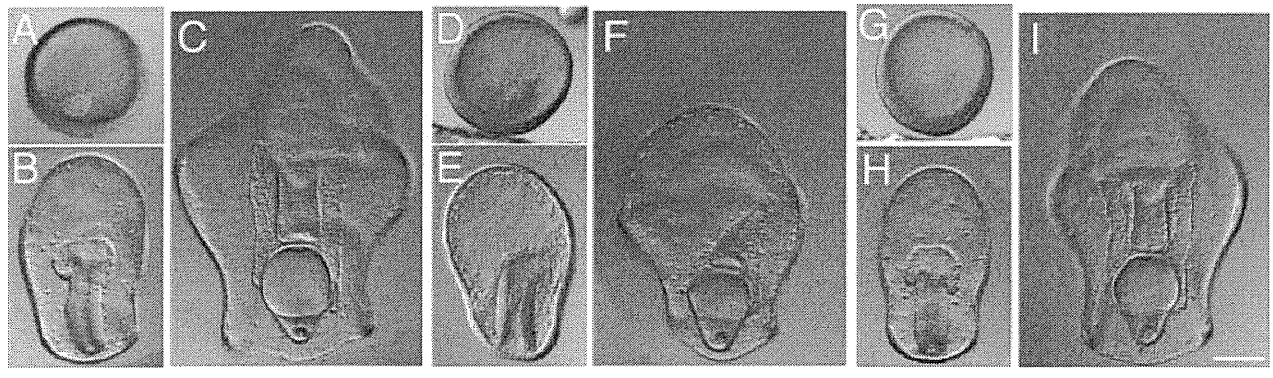

Fig. 6. Effects of injection of mesenchyme cells on later morphogenesis. **A–C**: Developmental stages in an embryo injected at the blastula stage with 40–50 mesenchyme cells (moderate cell number). **D–F**: Developmental stages in an embryo injected at the blastula stage with 150–200 mesenchyme cells (excess cell number). **G–I**: Developmental stages in an embryo sham injected (control) at the blastula stage. All panels show the Nomarski microscopic images merged with fluorescent images of live samples optically sectioned at the median plane. Developmental stages are as follows: blastula stage (just after mesenchyme cell injection; A,D); late-gastrula stage (1 day after injection; B,E); 3-day-old bipinnaria larva (2 days after injection; C,F). Although the image in E does not appear to have a four-fold increase in mesenchyme cells compared with B, this is simply a chance effect of optical sectioning. Notably, the embryos displayed variable morphogenetic phenotypes depending on the numbers of injected mesenchyme cells. See text for further explanation. Scale bar = 100 μm.

smaller than those in the sham control group (Fig. 6C,F,I). In all three experimental groups, innate mesenchyme cells showed normal ingression into the blastocoels of recipient embryos.

Total cell numbers were counted in 3-day-old bipinnaria larvae of all three experimental groups using the bacteria counter (Fig. 7). A remarkable difference in total cell numbers was found in the larvae derived from the injection experiment with the moderate number of mesenchyme cells compared with those from the other two experimental groups. The 3-day-old bipinnaria larvae produced by blastula embryos that had been injected with the moderate number of mesenchyme cells had approximately a 1.3-fold larger total cell number than those from the sham control group. The total cell numbers in the 3-day-old bipinnaria larvae produced by blastula embryos that had been injected with the excess number of mesenchyme cells were not significantly different from those of the sham control group (means ± SD; n = 3).

Injection of an Excess Number of Mesenchyme Cells Causes a Severe Condensation of a Fibrous Component the ECM

We previously reported that anomalous epithelial shape formation is closely related to an abnormal distribution of a fibrous component (4H11 fibers) of the ECM (Kaneko et al., 2005). These fibers are formed by a 370-kDa proteinaceous molecule that is recognized by the monoclonal antibody 4H11 Mab (Kaneko et al., 2005). Here, we investigated the distribution patterns of 4H11 fibers in the 3-day-old bipinnaria larvae of the three experimental groups described in Figure 6. No significant differences in the distribution of 4H11 fibers were present between the 3-day-old bipinnaria larvae injected with the moderate number of mesenchyme cells and those in the sham experiment (Fig. 8A,C). By contrast, 3-day-old bipinnaria larvae that had received an excess number of mesenchyme cells showed an unusual distribution of 4H11 fibers. The blastocoelic space of these larvae lacked 4H11 fibers in the anterior portion of the larval body (Fig. 8B, asterisk). Moreover, the injected mesenchyme cells were detected at every location that had 4H11 fibers but were never seen in regions lacking 4H11 fibers (Fig. 8B). This morphology was common to all the larvae in the excess mesenchyme cell experimental group.

A detailed analysis was carried out to compare the morphologies of 4H11 fibers in the region around the mouth of the blastocoelic spaces of larvae of the moderate and excess mesenchyme cell groups. In the moderate cell number group, this area was characterized by a V-shaped adoral ciliary band and the buccal cavity was located in the upper half of the mouth (Fig. 8D). The 4H11 fibers were present as a fine meshwork emanating from underneath the ectodermal wall in the vicinity of the esophagus (Fig. 8E). In contrast, in the excess cell number group, the adoral ciliary band had an oblong appearance and no buccal cavity was formed (Fig. 8F). Moreover, the esophagus connecting the mouth and stomach was present as a flattened duct (data not shown). At the same focal depth as the image shown in Figure 8E, 4H11 fibers were severely condensed and many of the injected mesenchyme cells were located there (Fig. 8G). Severe condensation of the 4H11 fibers was observed in all 3-day-old bipinnaria larvae of the excess mesenchyme cell group.

DISCUSSION

To elucidate the multiple functions performed by mesenchyme cells, we investigated the effects on epithelial cell proliferation of injection of mesenchyme cells into blastula embryos of the starfish *Asterina pectinifera*. Three principal findings were obtained in this study: (1) Embryos injected with 40 to 50 mesenchyme cells at the blastula stage had an approximately 1.3-fold larger total cell number at the mid-gastrula and 3-day-old bipinnaria stages than control embryos (Figs. 4, 7). (2) In two control groups that were either injected with epithelial cells or had a sham injection, the mid-gastrula embryos and 3-day-old bipinnaria larvae were composed of approximately 4,600 to 5,000 cells and 15,000 to 17,000 cells, respectively (Figs. 4, 7). (3) Injected mesenchyme cells did not undergo mitosis in the recipient embryos (Fig. 5). These data demonstrate that mesenchyme cells have the ability to induce epithelial cell proliferation, at least under our experimental conditions. This function might be opposed by other functions of the mesenchyme cells during starfish development, such as control of the ECM or clearance of the blastocoel (see Introduction).

The present study deals with an aspect of the epithelial–mesenchymal interaction. Our experimental approach had two particular features: first, the use of blastula embryos for injection, and, second, the use of a bacteria counter to determine cell numbers. The blastula embryo is a very simple body structure, characterized by a hollow sphere-like epithelial monolayer (Fig. 1). Up to the mid-gastrula stage, the embryo increases in total cell numbers with little apoptosis (Supp. Fig. S1). In addition, it is also sufficiently early in development to precede the appearance of innate mesenchyme cells at the mid-gastrula stage (Fig. 1). This last property is advantageous as it allowed us to obtain clear results without any "noise" due to innate mesenchyme cells. In addition, use of a bacteria counter allowed us to carry out a cytometric analysis on total cell numbers in individual embryos and larvae. In a preliminary experiment, a conventional cell counter was found to give barely acceptable estimates. The data we obtained from individual mid-gastrula embryos of a sham control experimental group (Fig. 4, see also Supp. Table S1) are comparable to those reported by Dan-Sohkawa and Satoh (1978) who reported an average total cell number of 4,908 using a squash preparation method.

Several studies have examined the influence of mesenchyme cells on epithelial cell proliferation. Most of these previous studies have been concerned with vertebrate organogenesis, such as of the pancreas (Bhushan et al., 2001), liver (Matsumoto et al., 2008), skin (Ming Kwan et al., 2004), salivary gland (Yamamoto et al., 2008), or tooth (Fukumoto et al., 2006). To the best of our knowledge, the present study is the first to describe the proliferative profile of epithelial cells during in vivo morphogenesis of a deuterostome invertebrate. Because the

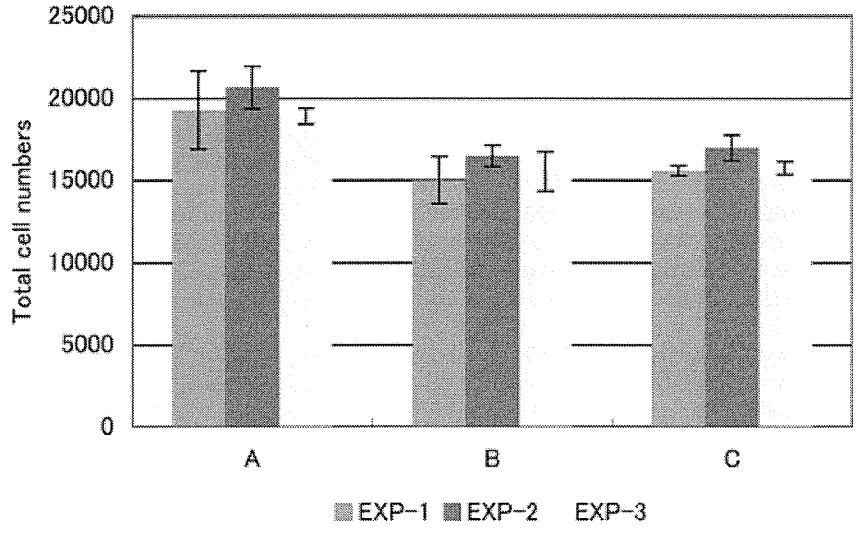

Fig. 7. Effect of mesenchyme cell injection into blastula embryos on total cell numbers of 3-day-old bipinnaria larva. **A–C**: The data are displayed according to the numbers of mesenchyme cells injected: 40–50 mesenchyme cells (moderate cell number; A); 150–200 mesenchyme cells (excess cell number; B); no cells injected (sham control; C). In three independent experiments, the total cell numbers represent the mean of six single larvae (standard deviation; bar). Notably, total cell numbers in larvae derived from embryos injected with the excess number of mesenchyme cells at the blastula stage were similar to those of the sham controls.

starfish is phylogenetically close to the origin of the chordate line, the function of mesenchyme cells described in this study might also be present in other invertebrate embryos of the chordate line. Our observations raise the question of how this function has been preserved during evolution.

Our quantitative data provide two insights into the morphogenetic function of mesenchyme cells as an inducer of epithelial cell proliferation. First, they provide some indication of the potential of a single mesenchyme cell to induce proliferation of epithelial cells. Blastula embryos injected with approximately 50 mesenchyme cells showed an increase in total cell number of approximately 1,500 cells at the mid-gastrula stage (Fig. 4, Supp. Table S1). Thus, each mesenchyme cell potentially induces proliferation of an average of 30 epithelial cells from the blastula to mid-gastrula stage. This potential induction is estimated as 90 epithelial cells at the 3-day-old

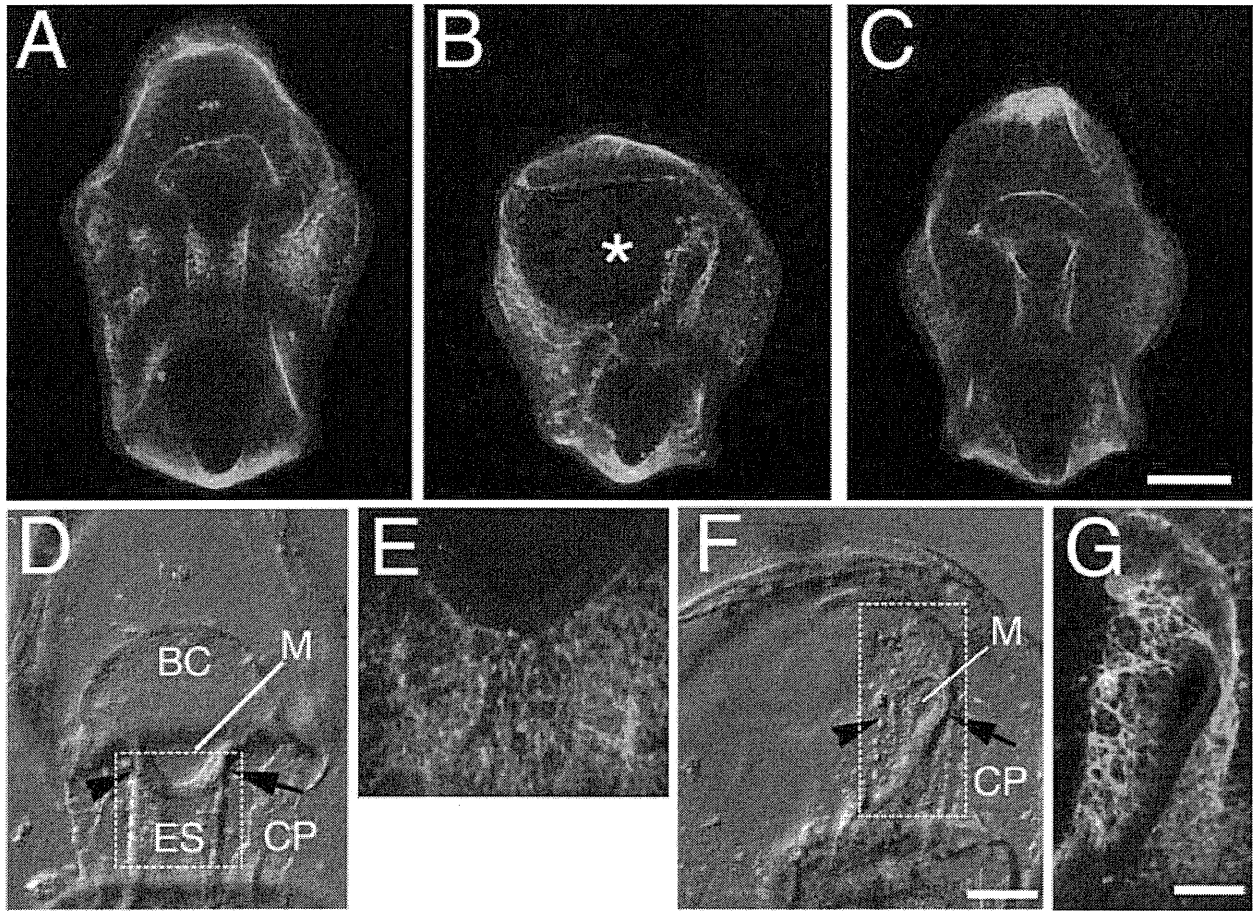

Fig. 8.

bipinnaria stage (Fig. 7, Supp. Table S2). Based on this analysis, a single mesenchyme cell can be inferred to govern proliferation of dozens of epithelial cells during at least a few days of development. One obvious caveat regarding this interpretation, however, is that our results were obtained from experiments involving injection of mesenchyme cells prepared in culture and not from transplantation experiments with innate mesenchyme cells.

Second, we need to consider the number of injected mesenchyme cells. Blastula embryos injected with the excess number of mesenchyme cells failed to show any increase in epithelial cell numbers (Fig. 7). This failure occurred without any indication of a disturbance to the appearance of the innate mesenchyme cells (Supp. Fig. S3). These observations suggest that the ratio of the number of mesenchyme cells to that of epithelial cells has a limiting influence on the ability of the epithelial cells to proliferate normally in interaction with mesenchyme cells during morphogenesis. It is of particular interest that failure of epithelial cell proliferation occurred concomitantly with abnormal morphogenesis in the larvae (Fig. 6). In particular, the blastocoelic space of the abnormal larvae lacked 4H11 fibers. Absence of 4H11 fibers from the blastocoelic spaces of larvae was also seen after treating starfish blastula embryos with the 4H11 Mab (see Fig. 6B of Kaneko et al., 2005). We also showed previously that some 4H11 fibers play a role as a flexible substrate that facilitates epithelial movements beneath ectodermal and endodermal walls (Kaneko et al., 2005). In this study, the altered distribution patterns of the 4H11 fibers was a direct consequence of an excess number of mesenchyme cells, which resulted in a change from the normal fine meshwork of 4H11 fibers to a severely condensed appearance (Fig. 8E,G). Moreover, many of the injected mesenchyme cells were observed to penetrate into the structures formed by the severely condensed 4H11 fibers (Fig. 8G). It is likely that the severe condensation of the 4H11 fibers renders them incapable of acting as a flexible substrate for epithelial movement and thus is an underlying cause of the failure of epithelial morphogenesis and epithelial cell proliferation. Our analyses suggest that epithelial cell proliferation may be regulated by a close interaction of the proper number of mesenchyme cells with 4H11 fibers.

Our observations here also suggest that mesenchyme cells play a role as supportive cells for epithelial cells as they proliferate during morphogenesis. It is unclear, at present, to what extent innate mesenchyme cells interact with epithelial cells to induce proliferation, and, if so, for how long and at which times during development. Two important questions were identified from this study. The first concerns normal starfish developmental processes: do innate mesenchyme cells have a ubiquitous role in epithelial cell proliferation to grow the embryonic body or do they participate in specialized organogenesis? The second question that needs to be addressed is the underlying molecular mechanism(s) that determine how mesenchyme cells function as a promoter of epithelial cell proliferation during normal embryonic development.

Fig. 8. 4H11 fibers in embryos that had been injected with different numbers of mesenchyme cells. **A–C**: 4H11 Mab immunofluorescence microscopic images of paraformaldehyde (PFA) fixed 3-day-larvae that received the moderate number (A), excess number (B), or no (C) mesenchyme cells. Injected mesenchyme cells (red) are present within the 4H11 fibers. Notably, the blastocoelic space of the embryos in group (B) lacked 4H11 fibers (asterisk). **D,F**: Nomarski microscopic images of the anterior portion of A and B. The adoral ciliary band forms a V-shaped mouth. The arrow and arrowhead point to the adoral ciliary band on the left and right sides, respectively. BC, the buccal cavity; M, the mouth; CP, the coelomic pouch; ES, the esophagus. **E,G**: The positions of 4H11fibers are enclosed in the dotted rectangles in D and F. In G, it is notable that the 4H11 fibers not only display a severely condensed morphology, but also that many injected mesenchyme cells are located within the fibers. Photos in A to C and E and G are shown as stacked images consisting of 10 or 25 optical sections taken using a confocal microscope at the same laser intensity, respectively. Scale bars = 100 μm in A–C, 50 μm in D,F, 25 μm in E,F.

EXPERIMENTAL PROCEDURES

Embryos

Mature eggs were obtained from the ovaries of starfish (*Asterina pectinifera*) treated with 1-methyladenine (Kanatani, 1969), and were fertilized with diluted sperm from the testes. Fertilized eggs were allowed to develop until the blastula, mid-gastrula of 3 days-bipinnaria stages at 20°C in artificial seawater (ASW, Marineart SF-1, Tomita Pharmaceutical). For the purposes of this study, we defined the blastula stage as newly-hatched embryos, and the mid-gastrula stage as those with invagination of the archenteron halfway across the blastocoel and just before the appearance of mesenchyme cells. These developmental stages were reached at 16 hr and 24 hr after fertilization, respectively.

Injection of Mesenchyme Cells or Epithelial Cells

A pure population of mesenchyme cells for injection was prepared from cell cultures as described previously (Kaneko et al., 1995a). In brief, the cells were washed with ASW, then labeled with rhodamine B isothiocyanate-celite (RITC) in culture at room temperature (RT) for 2 hr (Ettensohn and McClay, 1988). The cells were washed with ASW and then dislodged from the culture dish using a rubber policeman. The epithelial cells for injection were obtained from late-gastrula embryos. The embryos were first labeled with RITC for 6 to 10 hr, by which time they had reached the late gastrula stage. They were washed with ASW and the epithelial cells were removed from the ectoderm as described previously (Kaneko et al., 1990). There was no evidence of fluorescence decay of the RITC label in the mesenchyme or epithelial cells during the next 3 days. Mesenchyme or epithelial cells were aspirated into a microneedle, and injected into the blastocoel of each blastula embryo as described previously (Kaneko et al., 2005). The numbers of injected mesenchyme or epithelial cells were counted as they were ejected from the microneedle. In the sham experiment, a

microneedle was pushed into the blastocoel and then removed without injecting any solution. Each injected embryo was separately placed in 2 ml of ASW in a 24-well multi-plate (Sumitomo Bakelite Co., Ltd.), and allowed to develop at 20°C to the desired developmental stages. They were analyzed using a laser scanning confocal microscope (Olympus FluoView FV300) equipped with a helium-argon laser.

Cytometric Analysis

Two methods were used for cell counting. First, 30 embryos were collected and briefly pretreated in dissociation medium containing 0.1% trypsin (DMET: 1.2 M glycine; 2 mM EDTA; 0.1% trypsin). This medium was then replaced with 100 μl of DMET, and the embryos were incubated at RT for 5 min. They were dissociated into single cells by aspiration with a micropipette, and cell numbers were counted using a Thoma hemocytometer (#A106, Sunlead Glass Corporation; SLGC, Japan). An estimate of the total cell number of each embryo was then made. In the second approach, total cell numbers were determined separately for each embryo or larva. The embryos were treated as above except that only 2 μl of DMET was used, and a Sigmacote (Sigma)-coated mouth pipette and bacteria counter (#A161, SLGC, Japan) were used. The bacteria counter is designed to allow determination of cell numbers even in a small volume of a live cell suspension.

BrdU Treatment

Immediately after injection with mesenchyme cells, some blastula embryos were cultured in 5-bromo-2′-deoxyuridine (5 μM; BrdU, Sigma) in ASW until the mid-gastrula stage when they were fixed.

Fixation and Staining

In some experiments, embryos were fixed with 4% paraformaldehyde (PFA) in ASW at RT for 20 min or at 4°C over night. After washing with phosphate-buffered saline containing 0.01% Triton X-100 (PBST), the PFA-fixed embryos were post-fixed with ice-cold acetone at −20°C for 15 min. In the experiment to assess the structure of the embryos, the fixed normal blastula and mid-gastrula embryos were incubated in RNase A (200 μg/ml; Boehringer Mannheim, Germany) at 37°C for 20 min to remove the cytoplasmic RNA that quenches nuclear fluorescence signals at these developmental stages. The embryos were then incubated in PBST containing 0.165 μM of fluorescein isothiocyanate (FITC)-labeled phalloidin (Sigma) and 1 μg/ml propidium iodide (PI; Sigma) at RT for 30 min. In the BrdU treatment experiment, the fixed mid-gastrula embryos were incubated with 2N HCl at RT for 2 hr. They were stained with FITC-conjugated rat anti-BrdU (1:20 dilution with PBST, Oxford Biotechnology Ltd.) at RT for 30 min. Analyses of the distribution pattern of 4H11 fibers and of the structure of the fibrous component of the extracellular matrix were performed using samples that were immunofluorescently stained with the 4H11 Mab as described previously (Kaneko et al., 2005). In each experiment, samples were washed three to five times with PBST at RT after staining. The embryos were mounted on tape spacer, and viewed under an Olympus laser scanning confocal microscope as described above.

ACKNOWLEDGMENTS

We thank members of the Asamushi Marine Biological Station of Tohoku University for supplying the starfish. We also thank Drs. Ritsu Kuraishi and Ryohei Furukawa, Keio University, for critical discussion, Dr. Katsuhiro Ohta (Department of Mathematics, Keio University) for critical suggestions regarding quantitative analyses in this study. G.H. was supported by a KLL Research Grant for Ph.D. Program (Keio University) and H.K. received a Keio Gijuku Fukuzawa Memorial Fund for the Advancement of Education and Research.

REFERENCES

Abed M, Crawford BJ. 1986. Ultrastructural aspects of the mouth formation in the starfish Pisaster ochraceus. J Morphol 188:239–250.

Bhushan A, Itoh N, Kato S, Thiery JP, Czernichow P, Bellusci S, Scharfmann R. 2001. Fgf10 is essential for maintaining the proliferative capacity of epithelial progenitor cells during early pancreatic organogenesis. Development 128:5109–5117.

Crawford BJ. 1990. Changes in the arrangement of the extracellular matrix, larval shape, and mesenchyme cell migration during asteroid larval development. J Morphol 206:147–161.

Crawford BJ, Abed M. 1983. The role of the basal lamina in mouth formation in the embryo of the starfish Pisaster ochraceus. J Morphol 176:235–246.

Crawford BJ, Chia FS. 1978. Coelomic pouch formation in the starfish Pisaster ochraceus (Echinodermata: Asteroidea). J Morphol 157:99–120.

Crawford BJ, Campbel SS, Remimer CL. 1997. Ultrastructure and synthesis of the extracellular matrix of Pisaster ochraceus embryos preserved by freeze substitution. J Morphol 232:133–153.

Dan-Sohkawa M, Satoh N. 1978. Studies on dwarf larvae developed from isolated blastomeres of the starfish. Asterina pectinifera. J Embryol Exp Morphol 46: 171–185.

Dan-Sohkawa M, Tamura G., Mitsui H. 1980. Mesenchyme cells in starfish development: effect of tunicamycin on their differentiation, migration and function. Dev Growth Differ 22:495–502.

Ettensohn CA, McClay DR. 1988. Cell lineage conversion in the sea urchin embryo. Dev Biol 125:396–409.

Fukumoto S, Miner JH, Ida H, Fukumoto E, Yuasa K, Miyazaki H, Hoffman MP, Yamada Y. 2006. Laminin alpha5 is required for dental epithelium growth and polarity and the development of tooth bud and shape. J Biol Chem 281: 5008–5016.

Furukawa R, Takahashi Y, Nakajima Y, Dan-Sohkawa M, Kaneko H. 2009. Defense system by mesenchyme cells in bipinnaria larvae of the starfish, Asterina pectinifera. Dev Comp Immunol 33: 205–215.

Kanatani H. 1969. Induction of spawning and oocyte maturation by L-methyl-adenine in starfishes. Exp Cell Res 57: 333–337.

Kaneko H, Takaichi S, Yamamoto M, Dan-Sohkawa M. 1990. Acellularity of starfish embryonic mesenchyme cells as shown in vitro. Development 109:129–138.

Kaneko H, Kawahara Y, Dan-Sohkawa M. 1995a. Primary culture of mesodermal and endodermal cells of the starfish embryo. Zoolog Sci 12:551–558.

Kaneko H, Okushima Y, Ishizuka M, Dan-Sohkawa M. 1995b. A simple method for introducing macromolecules into the blastocoel of living starfish embryos. Zoolog Sci 12:559–564.

Kaneko H, Okai M, Murabe N, Shimizu T, Ikegami S, Dan-Sohkawa M. 2005. Fibrous component of the blastocoelic extracellular matrix shapes epithelia in